6-1-1997

Interpretation of Ultraviolet Absorption Lines in SN 1006

A. J. S. Hamilton
University of Colorado Boulder

R. A. Fesen
Dartmouth College

C.-C. Wu
Space Telescope Science Institute

D. M. Crenshaw
University of Virginia

THE ASTROPHYSICAL JOURNAL, 482:838–856, 1997 June 1

INTERPRETATION OF ULTRAVIOLET ABSORPTION LINES IN SN 1006[1]

A. J. S. HAMILTON
JILA and Department of Astrophysical, Planetary and Atmospheric Sciences, Box 440, University of Colorado, Boulder, CO 80309; ajsh@dark.colorado.edu

R. A. FESEN
Department of Physics and Astronomy, 6127 Wilder Laboratory, Dartmouth College, Hanover, NH 03755; fesen@oak.dartmouth.edu

C.-C. WU
Computer Sciences Corporation, Space Telescope Science Institute, 3700 San Martin Drive, Baltimore, MD 21218; wu@stsci.edu

D. M. CRENSHAW
Computer Sciences Corporation, LASP, Code 681, NASA-GSFC, Greenbelt, MD 20771; hrsmike@hrs.gsfc.nasa.gov

AND

C. L. SARAZIN
Department of Astronomy, University of Virginia, Box 3818, Charlottesville, VA 22903-0818; cls7i@coma.astro.virginia.edu

Received 1996 June 6; accepted 1996 December 31

ABSTRACT

We present a theoretical interpretation of the broad silicon and iron ultraviolet absorption features observed with the *Hubble Space Telescope* (*HST*) in the spectrum of the Schweizer-Middleditch star behind the remnant of SN 1006. These features are caused by supernova ejecta in SN 1006.

We propose that the redshifted Si II 1260 Å feature consists of both unshocked and shocked Si II. The sharp red edge of the line at 7070 km s^{-1} indicates the position of the reverse shock, while its Gaussian blue edge reveals shocked Si with a mean velocity of 5050 km s^{-1} and a dispersion of 1240 km s^{-1}, which implies a reverse shock velocity of 2860 km s^{-1}. The measured velocities satisfy the energy jump condition for a strong shock, provided that all the shock energy goes into ions, with little or no collisionless heating of electrons.

The line profiles of the Si III and Si IV absorption features indicate that they arise mostly from shocked Si. The total mass of shocked and unshocked Si inferred from the Si II, Si III, and Si IV profiles is $M_{\rm Si} = 0.25 \pm 0.01\ M_\odot$ on the assumption of spherical symmetry. Unshocked Si extends upward from 5600 km s^{-1}. Although there appears to be some Fe mixed with the Si at lower velocities $\lesssim$7070 km s^{-1}, the absence of Fe II absorption with the same profile as the shocked Si II suggests little Fe mixed with Si at higher (before being shocked) velocities. The column density of shocked Si II is close to that expected for Si II undergoing steady state collisional ionization behind the reverse shock, provided that the electron to Si II ratio is low, from which we infer that most of the shocked Si is likely to be of a fairly high degree of purity, unmixed with other elements. We propose that the ambient interstellar density on the far side of SN 1006 is anomalously low compared to the density around the rest of the remnant. This would simultaneously explain the high velocity of the redshifted Si absorption, the absence of blueshifted Si absorption, and the low density of the absorbing Si compared to the high Si density required to produce the observed Si X-ray line emission.

We have reanalyzed the Fe II absorption lines and have concluded that the earlier evidence for high-velocity blueshifted Fe II extending to ~ -8000 km s^{-1} is not compelling. We interpret the blue edge on the Fe II profiles at -4200 km s^{-1} as the position of the reverse shock on the near side of SN 1006. The mass of Fe II inferred from the red edge of the Fe II profile is $M_{\rm Fe\,II} = 0.029 \pm 0.004\ M_\odot$ up to 7070 km s^{-1}, if spherical symmetry is assumed. The low ionization state of unshocked Si inferred from our analysis of the silicon features, Si II/Si $= 0.92 \pm 0.07$, suggests a correspondingly low ionization state of unshocked iron, with Fe II/Fe $= 0.66^{+0.29}_{-0.22}$. If this is correct, then the total mass of Fe up to 7070 km s^{-1} is $M_{\rm Fe} = 0.044^{+0.022}_{-0.013}\ M_\odot$ with a 3 σ upper limit of $M_{\rm Fe} < 0.16\ M_\odot$. Such a low ionization state and mass of iron is consistent with the recent observation of Fe III 1123 Å with the Hopkins Ultraviolet Telescope (HUT), which indicates Fe III/Fe II $= 1.1 \pm 0.9$ but conflicts with the expected presence of several tenths of a solar mass of iron in this suspected Type Ia supernova remnant. However, the inference from the present *HST* data is too indirect, and the HUT data are too noisy, to rule out a large mass of iron. Reobservation of the Fe III 1123 Å line at higher signal-to-noise ratio with *Far Ultraviolet Space Explorer* will be important in determining the degree of ionization and hence mass of iron in SN 1006.

Subject headings: ISM: kinematics and dynamics — shock waves — supernovae: individual (SN 1006) — supernova remnants — ultraviolet: ISM

[1] Based on observations made with the NASA/ESA *Hubble Space Telescope*, obtained at the Space Telescope Science Institute, which is operated by the Association of Universities for Research in Astronomy, Inc., under NASA contract NAS 5-26555.

1. INTRODUCTION

In two previous papers, we (Wu et al. 1993, 1997; hereafter WCFHS93, WCHFLS97) described *Hubble Space Telescope* (*HST*) FOS observations of the UV spectrum of the SM star (Schweizer & Middleditch 1980) that lies behind and close to the projected center of the remnant of SN 1006. In the present paper, we offer a theoretical interpretation of the broad silicon and iron UV absorption features observed with *HST*. These features are almost certainly caused by supernova ejecta in SN 1006, as originally proposed by Wu et al. (1983), who first observed the features with *IUE*.

Detailed theoretical analysis of the Fe II features observed with *IUE* has been presented previously by Hamilton & Fesen (1988, hereafter HF88). The main purpose of that paper was to try to explain the apparent conflict between the low $\approx 0.015\ M_\odot$ mass of Fe II inferred from the *IUE* observations of SN 1006 (Fesen et al. 1988) with the expected presence of several tenths of a solar mass of iron (Höflich & Khokhlov 1996) in this suspected Type Ia supernova remnant (Minkowski 1966; Schaefer 1996). HF88 demonstrated that ambient UV starlight and UV and X-ray emission from reverse-shocked ejecta could photoionize unshocked iron mainly to Fe III, Fe IV, and Fe V, resolving the conflict.

Recently, Blair, Long, & Raymond (1996) used the Hopkins Ultraviolet Telescope (HUT) to measure Fe III 1123 Å absorption in the spectrum of the SM star. They found Fe III/Fe II $= 1.1 \pm 0.9$, which neither confirms, nor excludes, the ratio Fe III/Fe II $= 2.6$ predicted by HF88.

The *HST* spectra, particularly the silicon features, prove to be a rich source of information beyond the reach of *IUE*'s capabilities. In the first half of this paper, §2, we analyze the Si absorption features. We find (§ 2.1) that the profile of the redshifted Si II 1260 Å feature, with its sharp red edge and Gaussian blue edge, appears to be attributable to the presence of both unshocked and shocked silicon. We then develop a chain of inferences, first about the reverse shock (§ 2.2) and collisionless heating (§ 2.3), then about the column density and mass (§§ 2.4, 2.7), purity (§ 2.5), and ionization state (§ 2.6) of the silicon. We argue (§ 2.8) that the ambient interstellar density on the far of SN 1006 is anomalously low compared to density around the rest of the remnant, which explains the high velocity of the redshifted Si, the absence of corresponding blueshifted Si (§ 2.9), and some other observational puzzles.

In the second half of the paper, § 3, we discuss the broad Fe II absorption features. WCFHS93 reported blueshifted Fe II absorption up to ~ -8000 km s^{-1}. Finding the presence of such high-velocity blueshifted absorption difficult to understand in the light of other observational evidence, we detail a reanalysis of the Fe II features in § 3.1. We conclude (§ 3.2) that the evidence for high-velocity blueshifted absorption is not compelling, and we propose (§ 3.3) that the sharp blue edge on the Fe II profiles at -4200 km s^{-1} represents the position of the reverse shock on the near side. In the remainder of the section, §§ 3.4–3.6, we address the issue of the ionization state and mass of the iron.

We attempt in this paper to construct a consistent theoretical picture, but there remain some discrepancies, and we highlight these in § 4. Section 5 summarizes the conclusions.

2. SILICON

There are three possibilities for the origin of the broad Si absorption features in the spectrum of the SM star, if it is accepted that these features arise from the remnant of SN 1006.

The first possibility is that the absorption arises from cool, dense, fast-moving knots of ejecta, as suggested by Fesen et al. (1988) and further discussed by Fesen & Hamilton (1988). However, there has been no significant change in the features over 12 yr, from the original detection of the features with *IUE* in 1982 (Wu et al. 1983), through their reobservation with *IUE* in 1986 and 1988 (Fesen & Hamilton 1988), up to the FOS observation with *HST* in 1994 (WCHFLS97). Furthermore, the relative strengths of the redshifted Si II 1260 Å, 1304 Å, and 1527 Å features are approximately proportional to their oscillator strengths times wavelengths, which indicates that the lines are not saturated. This constancy in time and lack of saturation argues against the absorption features being caused by small, dense knots. We do not consider this hypothesis further in this paper.

A second possibility is that the Si absorption is from shocked ejecta in which the collisional ionization timescale is so long that the observed low-ionization species Si II, Si III, and Si IV can survive. At first sight, the high ~ 5000 km s^{-1} velocity of the observed absorption makes this possibility seem unlikely, because shocked ejecta should be moving no faster than the velocity of gas behind the interstellar shock, which in the northwest sector of the remnant can be inferred from the 2310 km s^{-1} FWHM of the Balmer broad-line emission to be 1800–2400 km s^{-1} (this is 3/4 of the shock velocity), depending on the extent to which electron-ion equilibration takes place (Kirshner, Winkler, & Chevalier 1987; Long, Blair, & van den Bergh 1988; Smith et al. 1991; Raymond, Blair, & Long 1995). However, below we will conclude that it is likely that much, in fact most, of the Si absorption is from shocked ejecta and that the ISM surrounding SN 1006 may be quite inhomogeneous.

A third possibility is that the Si absorption arises from unshocked supernova ejecta freely expanding in SN 1006, which is consistent with the high velocity of the absorption. The low ionization state of the Si, predominantly Si II, with some Si III and Si IV, is at least qualitatively consistent with the expectations of models in which the unshocked ejecta are photoionized by ambient UV starlight and by UV and X-ray emission from shocked ejecta (HF88). Neutral Si is neither observed, e.g., at Si I 1845 Å, nor expected, since it should be quickly (~ 20 yr) photoionized by ambient UV starlight. Recombination is negligible at the low densities here. At the outset, therefore, this possibility seems most likely, and we pursue the idea further in the next subsection.

Fesen et al. (1988) pointed out that the redshifted Si II 1260 Å feature (at ~ 1280 Å) in the *IUE* data appeared to be somewhat too strong compared to the weaker redshifted Si II 1527 Å feature. The discrepancy appears to be confirmed by the *HST* observations (WCHFLS97). Fesen et al. proposed that some of the Si II 1260 Å feature may come from S II 1260, 1254, 1251 Å redshifted by ≈ 800 km s^{-1} relative to the Si II, a possibility also addressed by WCHFLS97. In the present paper, we regard the possibility of any significant contribution from S II as unlikely, notwithstanding the discrepancy between the Si II profiles. The oscillator strengths of the S II 1260, 1254, 1251 Å lines are $f = 0.01624, 0.01088,$

0.005453, whose combined strength is only 1/30 of the oscillator strength $f = 1.007$ of the Si II 1260 Å line (Morton 1991). In models of Type Ia supernovae, such as SN 1006 is believed to be, silicon and sulfur occur typically in the same region of space, with a relative abundance of Si:S $\approx$ 2:1 (see, e.g., Nomoto, Thielemann, & Yokoi 1984). Thus, S II might be expected to contribute only $\sim$1/60 of the optical depth of Si II in the 1260 Å feature, assuming a similar ionization state of Si and S. In the remainder of this paper, we ignore any possible contribution of S II to the Si II 1260 Å feature. In this we follow Wu et al.'s (1983) original identification of the 1280 Å absorption feature as redshifted Si.

2.1. *The Redshifted* Si II 1260 Å *Feature*

Given that SN 1006 shows a well-developed interstellar blast wave in both radio (Reynolds & Gilmore 1986, 1993) and X-rays (Koyama et al. 1995; Willingale et al. 1996), it is inevitable that a reverse shock must be propagating into any unshocked ejecta.

If the observed UV Si absorption is from unshocked ejecta, then there should be a sharp cutoff in the line profile at the expansion velocity of the reverse shock, because the shock should "instantaneously" decelerate the ejecta to lower bulk velocity. In fact the Si II 1260 Å feature does show a steep red edge at 7070 $\pm$ 50 km s^{-1}, albeit with a possible tail to higher velocities. Tentatively, we take the presence of the steep red edge as evidence that at least some of the Si II is unshocked.

Once shocked, how long will Si II last before being collisionally ionized to higher levels? The ionization timescale of Si II entering the reverse shock can be inferred from the optical depth of the Si II 1260 Å absorption just inside its steep red edge at 7070 km s^{-1}, which putatively represents the position of the reverse shock. In freely expanding ejecta where radius equals velocity times age, $r = vt$, the column density per unit velocity dN/dv of any species is equal to the density $n = dN/dr$ times age t. For freely expanding ejecta, the optical depth τ in a line of wavelength λ and oscillator strength f is then proportional to nt:

$$\tau = \frac{\pi e^2}{m_e c} f\lambda \frac{dN}{dv} = \frac{\pi e^2}{m_e c} f\lambda n t \, . \quad (1)$$

The optical depth of the Si II 1260.4221 Å line ($f = 1.007$; Morton 1991) just inside its steep red edge is $\tau \approx 1$. This implies, from equation (1), a preshock Si II density times age of $n_{\rm Si\,II}^{\rm presh} t = 3.0 \times 10^6$ cm^{-3} s. The postshock Si II density times age would then be 4 times higher for a strong shock, $n_{\rm Si\,II} t = 1.2 \times 10^7$ cm^{-3} s. At a collisional ionization rate for Si II of $\langle \sigma v \rangle_{\rm Si\,II} = 6 \times 10^{-8}$ cm^{3}s^{-1} (Lennon et al. 1988; see § 2.5 below for further discussion of this rate), the ratio of the Si II ionization timescale $t_{\rm Si\,II} \equiv (n_e \langle \sigma v \rangle_{\rm Si\,II})^{-1}$ to the age of the remnant, t, is (the following estimate is revised below; eq. [3])

$$\frac{t_{\rm Si\,II}}{t} = \frac{1}{n_e t \langle \sigma v \rangle_{\rm Si\,II}} = \frac{n_{\rm Si\,II}}{n_e} \frac{1}{n_{\rm Si\,II} t \langle \sigma v \rangle_{\rm Si\,II}} = 1.4 \frac{n_{\rm Si\,II}}{n_e} \, . \quad (2)$$

Since the ratio $n_e/n_{\rm Si\,II}$ of electron to Si II density in the postshock gas should be greater than but of order unity, this estimate (eq. [2]) indicates that the collisional timescale of Si II is of the order of the age of the remnant. It follows that shocked Si II is likely also to contribute to the observed Si II absorption.

Shocked Si II will be decelerated by the reverse shock to lower velocities than the freely expanding unshocked ejecta. Shocked Si II should have a broad thermal profile, unlike the unshocked Si II. Examining the redshifted Si II 1260 Å profile, we see that the blue edge extends down to about + 2500 km s^{-1}, with a shape that looks Gaussian. Fitting the blue edge to a Gaussian, we find a best fit to a Gaussian centered at 5050 km s^{-1}, with a dispersion (standard deviation) of $\sigma = 1240$ km s^{-1}. This fit is shown in Figure 1. Having started from the point of view that the Si II was likely to be unshocked, we were surprised to see that, according to the fit, it is shocked Si II that causes most of the absorption, although an appreciable quantity of unshocked Si is also present, at velocities extending upward from 5600 km s^{-1}. The slight tail of Si II absorption to high velocities >7070 km s^{-1} is naturally produced by the tail of the Gaussian profile of the shocked Si II.

The estimate (eq. [2]) of the collisional ionization timescale of Si II presumed that all the Si II 1260 Å absorption was from unshocked Si II, whereas the picture now is that only some of the absorption is from unshocked Si II. According to the fit in Figure 1, the optical depth of unshocked Si II at the reverse shock front is $\tau = 0.56 \pm 0.07$, a little over half that adopted in equation (2), so a revised estimate of the ionization timescale of Si II is not quite double that of the original estimate (eq. [2]):

$$\frac{t_{\rm Si\,II}}{t} = 2.5 \frac{n_{\rm Si\,II}}{n_e} \, . \quad (3)$$

Evidently the conclusion remains that the ionization timescale of Si II is comparable to the age of the remnant.

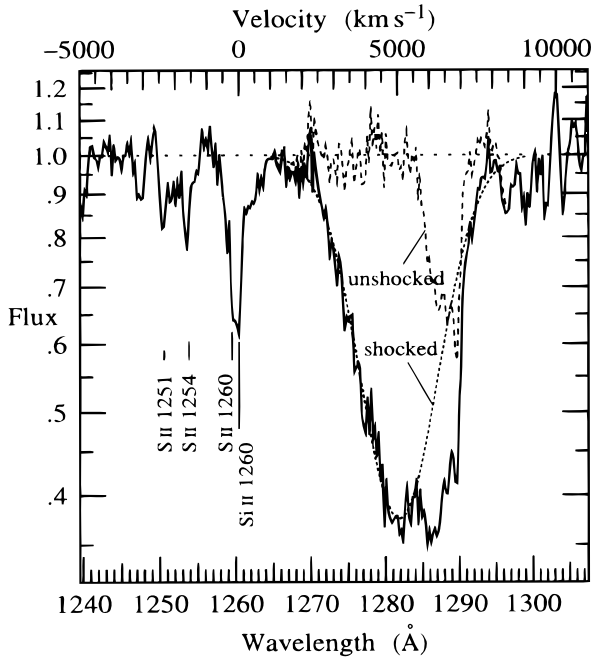

FIG. 1.—*HST* G130H spectrum relative to the stellar continuum around the redshifted Si II 1260.4221 Å feature, showing the best-fit Gaussian profile of shocked Si II and the residual unshocked Si II. Upper axis shows velocity in the rest frame of the Si II line. Measured parameters of the feature are given in Table 1. As elsewhere in this paper, we assume a stellar continuum that is linear in log F–log λ, and we fit the continuum to ostensibly uncontaminated regions around the line. The adopted stellar continuum is log F = log (4.1 × 10^{-14} ergs s^{-1} cm^{-2} Å^{-1}) − 2.3 log (λ/1260 Å).

2.2. *Shock Jump Conditions*

The fitted profile of the Si II 1260 Å feature in Figure 1 includes both unshocked and shocked components. The consistency of the fitted parameters can be checked against the jump conditions for a strong shock. The shock jump conditions predict that the three-dimensional velocity dispersion $3^{1/2}\sigma$ of the ions should be related to the deceleration Δv of the shocked gas by energy conservation

$$3^{1/2}\sigma = \Delta v \tag{4}$$

provided that all the shock energy goes into ions. The observed dispersion is

$$3^{1/2}\sigma = 3^{1/2} \times (1240 \pm 40 \text{ km s}^{-1}) = 2140 \pm 70 \text{ km s}^{-1} \tag{5}$$

(quoted uncertainties throughout this paper are 1 σ) while the observed deceleration is

$$\begin{aligned} \Delta v &= (7070 \pm 50 \text{ km s}^{-1}) - (5050 \pm 60 \text{ km s}^{-1}) \\ &= 2020 \pm 80 \text{ km s}^{-1} . \end{aligned} \tag{6}$$

These agree remarkably well, which encourages us to believe that this interpretation is along the right lines. The reverse shock velocity, v_s, corresponding to the observed dispersion is

$$v_s = (16/3)^{1/2}\sigma = 2860 \pm 100 \text{ km s}^{-1} . \tag{7}$$

We prefer to infer the shock velocity from the observed dispersion rather than from the observed deceleration Δv, since the latter may underestimate the true deceleration, if, as is likely, the shocked Si is moving on average slightly faster than the immediate postshock gas (see below).

The predicted equality (4) between the deceleration and ion dispersion holds provided that all the shock energy goes into ions and that the bulk velocity and dispersion of the ions in the shocked gas are equal to their postshock values. Since the shocked Si II can last for a time comparable to the age of the remnant (eq. [3]), it cannot be assumed automatically that the bulk velocity and dispersion of the observed Si II ions are necessarily equal to those immediately behind the reverse shock front. We discuss first the issue of the bulk velocity, then the dispersion, and finally the question of collisionless heating in § 2.3.

Consider first the bulk velocity of the shocked ions. In realistic hydrodynamic models, the velocity of shocked gas increases outward from the reverse shock. Indeed, the fact that the observed dispersion $3^{1/2}\sigma$ is larger than the observed deceleration Δv by 120 ± 130 km s^{-1} (the uncertainty here takes into account the correlation between the uncertainties in σ and Δv) is consistent with the notion that the shocked Si II is moving on average 120 ± 130 km s^{-1} faster than the immediate postshock gas. This modest velocity is consistent with expectations from one-dimensional hydrodynamic simulations appropriate to SN 1006 (see HF88, Fig. 2), according to which shocked ejecta remain relatively close to the reverse shock front. However, the deceleration of ejecta is generally Rayleigh-Taylor unstable (see, e.g., Chevalier, Blondin, & Emmering 1992), which instabilities could have caused shocked Si II to appear at velocities many hundred km s^{-1} faster than the immediate postshock gas. Since the observations do not show this, it suggests, though by no means proves, either that Rayleigh-Taylor instabilities are not very important, or perhaps that the line of sight through SN 1006 to the SM star happens to lie between Rayleigh-Taylor plumes.

What about the ion dispersion? If there were a range of ion dispersions in the shocked gas, then the line profile would tend to be more peaked and have broader wings than a simple Gaussian. The observed profile of the blue edge of the redshifted Si II 1260 Å feature is consistent with a Gaussian, which suggests, again weakly, that the ion dispersion does not vary by a large factor over the bulk of the shocked Si II.

While the observations agree well with the simplest possible interpretation, it is certainly possible to arrange situations in which a combination of Rayleigh-Taylor instabilities, spatially varying ion dispersion, and collisionless heating conspire to produce fortuitous agreement of the observations with the jump condition (4).

2.3. *Collisionless Heating*

The shock jump condition (4) is valid provided that all the shock energy goes into the ions, rather than into electrons, magnetic fields, or relativistic particles. The timescale for equilibration by Coulomb collisions between electrons and ions or between ions and ions is much longer than the age of SN 1006. However, collisionless processes in the shock may also transfer energy, and the extent to which these may accomplish equilibration remains uncertain (see Laming et al. 1996 for a recent review). The prevailing weight of evidence favors little if any collisionless heating of electrons in the fast shocks in SN 1006. Raymond et al. (1995) find similar velocity widths in emission lines of H I (Lyβ), He II, C IV, N V, and O VI observed by HUT from the interstellar shock along the northwest sector of SN 1006. They conclude that there has been little equilibration between ions, though this does not rule out substantial electron heating. From the same data, Laming et al. (1996) argue that the ratio of C IV (which is excited mainly by protons) to He II (which is excited mainly by electrons) is again consistent with little or no electron-ion equilibration. Koyama et al. (1995) present spectral and imaging evidence from *ASCA* that the high-energy component of the X-ray spectrum of SN 1006 is nonthermal synchrotron radiation, which obviates the need for collisionless electron heating (see also Reynolds 1996).

The results reported here, equations (5) and (6), tend to support the conclusion that virtually all the shock energy is deposited into the ions. If some of the shock energy were channeled into electrons, magnetic fields, or relativistic particles, then the ion dispersion would be lower than predicted by the observed deceleration, whereas the opposite is observed—the ion dispersion is slightly higher.

2.4. *Column Density and Mass of* Si II

The numbers given in this subsection are summarized in Table 1. Quoted 1 σ uncertainties in column densities and masses here and throughout this paper exclude uncertainties in oscillator strengths and systematic uncertainties from placement of the continuum. The uncertainties in the oscillator strengths of Si II 1260 Å are 17% and of Si III 1206 Å and Si IV 1394, 1403 Å are 10% (Morton 1991). The systematic uncertainties arising from placement of the continuum are difficult to assess in the absence of a reliable observational or theoretical stellar template but could easily exceed the statistical uncertainty, perhaps by a factor of 2 or more.

TABLE 1

PARAMETERS MEASURED FROM REDSHIFTED Si II 1260 Å FEATURE

Parameter	Value
Expansion velocity into reverse shock	7070 ± 50 km s^{-1}
Mean velocity of shocked Si II	5050 ± 60 km s^{-1}
Dispersion of shocked Si II	1240 ± 40 km s^{-1}
Reverse shock velocity	2860 ± 100 km s^{-1}
Lower edge of unshocked Si II	5600 ± 100 km s^{-1}
Preshock density of Si II	$5.4 \pm 0.7 \times 10^{-5}$ cm^{-3}
Column density of shocked Si II	$9.0 \pm 0.3 \times 10^{14}$ cm^{-2}
Column density of unshocked Si II	$1.5 \pm 0.2 \times 10^{14}$ cm^{-2}
Column density of all Si II	$10.5 \pm 0.1 \times 10^{14}$ cm^{-2}
Mass of shocked Si II	$0.127 \pm 0.006\ M_\odot$
Mass of unshocked Si II	$0.017 \pm 0.002\ M_\odot$

NOTES.—(1) Masses assume spherical symmetry. For simplicity, velocities and masses have not been adjusted for the small offset of the SM star from the projected center of the remnant. (2) All uncertainties are statistical 1 σ errors (see §2.4 for a more detailed specification of the uncertainties).

In all fits, the formal χ^2 per degree of freedom computed from photon-counting noise, as tabulated in the *HST* spectral data file, exceeded the expected value of 1 by a factor that was 1.7 for Si II 1260 Å, 2.1 for Si III 1206 Å, and 2.8 for Si IV 1394, 1403 Å. This suggests either that there is some additional source of noise—perhaps unresolved stellar lines—or else that the noise is correlated between adjacent spectral bins. Whatever the case, all uncertainties quoted in this paper are based on the higher noise level inferred from the fits, rather than on the nominal photon noise.

The column density of shocked and unshocked Si II follows from integrating over the line profiles shown in Figure 1. The column density $N_{\rm Si\,II}^{\rm sh}$ of shocked Si II is

$$N_{\rm Si\,II}^{\rm sh} = \frac{m_e c}{\pi e^2 f\lambda}(2\pi)^{1/2}\sigma\tau_0 = 9.0 \pm 0.3 \times 10^{14}\ {\rm cm}^{-2}\ , \quad (8)$$

where $\tau_0 = 0.98 \pm 0.02$ is the optical depth at line center of the fitted Gaussian profile of the shocked Si II, and the factor $(2\pi)^{1/2}\sigma$ comes from integrating over the Gaussian profile. The profile of unshocked Si II is the residual after the shocked Si II is subtracted from the total, and we measure its column density $N_{\rm Si\,II}^{\rm unsh}$ by integrating the unshocked profile over the velocity range 5600–7200 km s^{-1}:

$$N_{\rm Si\,II}^{\rm unsh} = \frac{m_e c}{\pi e^2 f\lambda}\int \tau^{\rm unsh}\, dv = 1.5 \pm 0.2 \times 10^{14}\ {\rm cm}^{-2} \quad (9)$$

where the uncertainty is largely from uncertainty in the fit to the shocked Si II. Integrating the full Si II profile over 1000–8200 km s^{-1} yields the total column density of Si II

$$N_{\rm Si\,II} = 10.5 \pm 0.1 \times 10^{14}\ {\rm cm}^{-2}\ , \quad (10)$$

where the uncertainty is from photon counts and is smaller than the uncertainties in either of the shocked or unshocked Si II column densities individually (because there is some uncertainty in allocating the total column density between the shocked and unshocked components). WCHFLS97 quote a Si II column density of $6.7 \pm 0.6 \times 10^{14}$ cm^{-2}, which is substantially smaller than the above value. WCHFLS97's column density is measured from the weaker Si II 1527 Å feature because of concern over possible contamination of the Si II 1260 Å feature by S II 1260, 1254, 1251 Å. Here we take the point of view that the column density of the stronger feature is more reliable than that of the weaker line, especially since the latter is partially confused by C IV and C I absorption (see WCHFLS97, Fig. 2). The discrepancy in the column densities highlights the fact that ambiguities in the stellar continuum comprise a source of systematic uncertainty that may dominate the statistical uncertainty.

The masses of shocked and unshocked Si II can also be inferred from the observed Si II 1260 Å profile, if it is assumed that the Si was originally ejected spherically symmetrically. In § 2.8, we will argue that the absence of blueshifted Si II absorption can be explained if the reverse shock has passed entirely through the Si on the near side of SN 1006 and Si has been collisionally ionized to high ion stages. Thus the absence of blueshifted Si II need not conflict with spherical symmetry of Si ejected in the supernova explosion. If the shocked ejecta are taken to lie in a thin shell at a free expansion radius of $v = 7200$ km s^{-1} (slightly outside the position of reverse shock—see the argument in paragraph 3 of § 2.2), then the mass of shocked Si II is

$$M_{\rm Si\,II}^{\rm sh} = 4\pi m_{\rm Si\,II}(vt)^2 N_{\rm Si\,II}^{\rm sh} = 0.127 \pm 0.006\ M_\odot\ , \quad (11)$$

where the uncertainty includes only the uncertainty in the column density of shocked Si II. This value should perhaps be modified to $M_{\rm Si\,II}^{\rm sh} = 0.13 \pm 0.01\ M_\odot$ to allow for uncertainty in the radial position of the shocked Si II. The mass of unshocked Si II is an integral over the unshocked line profile

$$M_{\rm Si\,II}^{\rm unsh} = 4\pi m_{\rm Si\,II} t^2 \int v^2\, dN_{\rm Si\,II}^{\rm unsh} = 0.017 \pm 0.002\ M_\odot\ , \quad (12)$$

where the uncertainty is largely from uncertainty in the fit to the shocked Si II.

2.5. *Purity of Shocked* Si

We show below that the observed column density of Si II is close to the column density that would be predicted under the simple assumption of steady state collisional ionization downstream of the shock (note that recombination is negligible). Now the assumption of steady state ionization is surely false, since the timescale to ionize Si II is comparable to the age of the remnant, equation (3). Below, we will argue that the effect of non–steady state is generally such as to reduce the column density below the steady state value. The constraint that the observed column density should be less than or comparable to the steady state value then leads to an upper limit on the electron-to-ion ratio, equation (14). The fact that this upper limit is not much greater than unity leads to the interesting conclusion that the bulk of the observed shocked Si II must be fairly pure, since admixtures of other elements would increase the electron to ion ratio above the limit.

If the postshock number density of Si II ions is $n_{\rm Si\,II}$ (which is 4 times the preshock number density), then at shock velocity v_s, the number of Si II ions entering the reverse shock per unit area and time is $n_{\rm Si\,II} v_s/4$. The Si II ions are collisionally ionized by electrons in the shocked gas at a rate $n_e\langle\sigma v\rangle_{\rm Si\,II}$ ionizations per unit time. For $v_s = 2860$ km s^{-1} and $\langle\sigma v\rangle_{\rm Si\,II} = 6.1 \times 10^{-8}{\rm cm}^3{\rm s}^{-1}$, it follows that the column density $N_{\rm Si\,II}^{\rm steady}$ of shocked Si II in steady state should be

$$N_{\rm Si\,II}^{\rm steady} = \frac{n_{\rm Si\,II} v_s}{4 n_e \langle\sigma v\rangle_{\rm Si\,II}} = 1.2 \times 10^{15}\ {\rm cm}^{-2}\,\frac{n_{\rm Si\,II}}{n_e}\ . \quad (13)$$

If, as will be argued below, the actual (non–steady state) column density (eq. [8]) of shocked Si II is less than or comparable to the steady state value (eq. [13]), then the mean ratio of electron to Si II density in the shocked gas

satisfies

$$\frac{n_e}{n_{\rm Si\ II}} \lesssim 1.3 \ . \tag{14}$$

The ratio must of course also satisfy $n_e/n_{\rm Si\ II} \geq 1$, since each Si II ion itself donates one electron. Such a low value (eq. [14]) of the electron–to–Si II ratio in the shocked Si II would indicate that the bulk of the shocked Si II must be of a rather high degree of purity, since the presence of significant quantities of other elements or higher ionization states of Si would increase the number of electrons per Si II ion above the limit (14). Indeed, even if the Si II entering the shock were initially pure, ionization to Si III and higher states would release additional electrons. In steady state, the mean electron–to–Si II ratio experienced by Si II during its ionization from an initially pure Si II state is $n_e/n_{\rm Si\ II} = 1.5$, already slightly larger than the limit (14).

The limit (14) on the electron–to–Si II ratio is so low as to make it difficult to include even modest quantities of other elements with the silicon. This may be a problem. While Si is generally the most abundant element in Si-rich material produced by explosive nucleosynthesis, other elements, notably sulfur, usually accompany the silicon. For example, the deflagrated white dwarf model W7 of Nomoto et al. (1984) contains 0.16 $M_\odot$ of Si mostly in a layer that is about 60% Si, 30% S by mass. At this elemental abundance, and assuming similar ionization states for all elements, the expected mean electron–to–Si II ratio in steady state would be $n_e/n_{\rm Si\ II} = 1.5/0.6 = 2.5$, almost twice the limit given by equation (14). Because of this potential difficulty, we discuss carefully below how robust is the constraint (14). First we address the accuracy of the predicted value (eq. [13]) of the steady state column density, and then we discuss the non–steady state case.

The electron–to–Si II ratio could be increased if the predicted steady state column density (eq. [13]) were increased, either by increasing the shock velocity v_s or by reducing the collisional ionization rate $\langle \sigma v \rangle_{\rm Si\ II}$. We consider the former first, then the latter. The shock velocity $v_s = 2860$ km s^{-1} is inferred from the observed ion dispersion in the Si II 1260 Å line, equation (7). This should give a fair estimate of the mean shock velocity of the observed shocked Si II, except for a small correction from the fact that the ion dispersion (temperature) in the past would have been higher because of adiabatic expansion of the remnant. Moffet, Goss, & Reynolds (1993) find that the global radius R of the radio remnant is currently increasing with time according to $R \propto t^{0.48 \pm 0.13}$. If the ambient ISM is assumed to be uniform, this indicates that the pressure in the remnant is varying with time as $P \propto (R/t)^2 \propto t^{-1.04 \pm 0.26}$; hence that the temperature is varying in Lagrangian gas elements as $T \propto P^{2/5} \propto t^{-0.42 \pm 0.10}$; and hence that the ion dispersion is varying as $\sigma \propto T^{1/2} \propto t^{-0.21 \pm 0.05}$, a rather weak function of time. If one supposes that the observed Si II was shocked on average when SN 1006 was, say, half its current age, then the dispersion, hence the reverse shock velocity, could have been $\sim$20% higher than at present. The steady state column density (eq. [13]) would then be $\sim$20% higher, and the constraint on the electron–to–Si II ratio (eq. [14]) would be relaxed slightly to $n_e/n_{\rm Si\ II} \lesssim 1.5$.

The collisional ionization rate $\langle \sigma v \rangle_{\rm Si\ II} = 6.1 \times 10^{-8}$ cm^{3}s^{-1} used in equation (13) comes from integrating the cross sections of Lennon et al. (1988) over a Maxwellian distribution of electrons at a temperature of 83 eV. The quoted error in the cross sections is 60%, the large uncertainty arising from the fact that the cross sections for Si II are derived from isoelectronic scaling rather than from real data. Reducing the ionization rate by 0.2 dex would relax the constraint (14) to $n_e/n_{\rm Si\ II} \lesssim 2.0$.

The temperature of 83 eV used in the collisional ionization rate above is the temperature reached by electrons as a result of Coulomb collisions with Si II ions over the collisional ionization timescale of Si II. The assumption here that there is no collisionless heating of electrons in the shock is in accordance with the arguments given in § 2.3. Actually, the ionization rate of Si II by electron impact, as derived from the cross sections of Lennon et al., has a broad maximum at an electron temperature of $\sim$200 eV and varies over only 5–7 $\times$ 10^{-8} cm^3 s^{-1} for electron temperatures 40–1000 eV. Thus uncertainty in the electron temperature does not lead to much uncertainty in the collisional ionization rate, unless there is substantial collisionless heating of electrons to temperatures much higher than 1 keV.

We have argued against significant collisionless electron heating in § 2.3. However, if collisionless electron heating to temperatures greater than 1 keV did occur, it would imply both a higher shock velocity, since the observed ion dispersion would underestimate the shock energy, and a lower collisional ionization rate, both of which act to increase the steady state column density (eq. [13]). Thus, collisionless electron heating, if it occurs, would allow a larger electron–to–Si II ratio than given by equation (14).

We now turn to the argument that in a non–steady state situation, as here, the column density of shocked Si II is likely to be less than the steady state column density (eq. [13]), which leads to the constraint (14) on the mean electron–to–Si II ratio in the shocked Si II. In the first place, simply truncating the Si at some point downstream of the shock will give a lower column density than the steady state value. Second, geometric effects tend to reduce the column density below the steady state value. That is, the column density of Si II is diluted by the squared ratio $(r_s/r)^2$ of the original radius r_s of the gas at the time it was shocked to the present radius r ($>r_s$) of this shocked gas. Third, if the density profile of shocked Si at the present time increases outward, then the faster ionization of the denser, earlier shocked, gas reduces its column density per interval of ionization time, and the net column density is again lower than steady state (a more rigorous demonstration of this is given in the Appendix). Conversely, if the density profile of shocked Si decreases outward, then the net column density can be higher than steady state but only if the flow is allowed to continue for sufficiently longer than a collisional ionization time. However, according to equation (3), the ionization timescale at the present Si II density is comparable to the age of the remnant, and the ionization timescale would be longer at lower density, so there is not much room for increasing the column density this way either.

So is there any way that the actual column density of Si II could be higher than the steady state value? Clearly yes, given sufficient freedom with the density profile of shocked Si. For example, one possibility is that there is a "hump" in the shocked Si II density profile, such that the density increases outward of the present position of the reverse shock front but then declines at larger radii. Some tuning is required to ensure that the density on both near and far

sides of the hump is high enough to produce significant column density but not so high as to ionize Si above Si II. The higher the column density, the more fine-tuning is required.

We thus conclude that while some violation of the limit (14) on the mean electron–to–Si II ratio in the shocked Si II is possible, greater violations, exceeding, say, a factor of 2, are less likely. It then follows that the bulk of the shocked Si II is likely to be of a fairly high degree of purity. In particular, there is unlikely to be much iron mixed in with the shocked silicon, a conclusion that is consistent with the absence of Fe II absorption with the same profile as the shocked Si II, as discussed in § 3.4. To avoid misunderstanding, this statement refers only to the shocked Si II: iron could be mixed with the unshocked Si, and indeed the absorption profile of Fe II, Figure 6 below, does suggest that there is some Fe mixed with unshocked Si.

2.6. Si III *and* Si IV *Line Profiles*

Given that shocked Si II apparently persists for a time comparable to its ionization time, it is difficult to avoid producing an appreciable quantity of Si III and Si IV as the result of collisional ionization of Si II in the shocked ejecta. We thus conclude that it is likely that most of the observed Si III and Si IV absorption arises from shocked ejecta. This is consistent with the observed line profiles, as will now be discussed.

Figures 2 and 3 show fits to the redshifted Si III 1206 Å and Si IV 1394, 1403 Å features using as templates the shocked and unshocked profiles of Si II 1260 Å shown in Figure 1. Table 2 gives the fitted column densities of shocked and unshocked Si III and Si IV, expressed relative to the respective best-fit column densities of shocked and unshocked Si II given in Table 1.

The Si III 1206 Å profile appears to be mostly shocked. There is some indication of unshocked Si III over 5500–7000 km s^{-1} at the 2 σ level, Table 2, as suggested by the residual profile after subtraction of shocked Si III plotted in Figure 2. The dispersion of the fitted Gaussian profile of the Si III, if allowed to be a free parameter, is 1290 ± 60 km s^{-1} if unshocked Si III is excluded, or 1210 ± 60 km s^{-1} if unshocked Si III is admitted, which are in good agreement with the 1240 ± 40 km s^{-1} dispersion of the Si II.

The profile of the Si IV 1394, 1403 Å feature, Figure 3, is consistent with containing no unshocked Si IV. The absence of unshocked Si IV accounts for the difference between the profiles of the Si II 1260 Å and Si IV features remarked by WCHFLS97 and shown clearly in their Figure 2. If the line center and width of the Gaussian pair fitted to the Si IV 1394, 1403 Å doublet are allowed to be free, then the center remains close to 5050 km s^{-1}, the same as for Si II 1260 Å, but the best-fit dispersion of the Si IV is 1700 ± 100 km s^{-1}, which is 4.5 σ higher than the 1240 km s^{-1} dispersion of Si II 1260 Å. The broader dispersion suggests that the Si IV may be in slightly lower density gas than the Si II, since the pressure is presumably the same for both. It is not clear, however, that the observed difference in velocity width between Si IV and Si II is real. One problem is that the continuum around Si IV appears less well defined than for the Si II and Si III features. As elsewhere in this paper, we assume a stellar continuum that is linear in log F– log λ, but in fact there is a hint of curvature, a large-scale depression in the continuum around Si IV 1394, 1403 Å (see WCHFLS97, Fig. 1). If we have systematically misjudged the continuum, then it is possible that we have underestimated the uncertainties in the parameters of Si IV given Table 2, perhaps by as much as a factor of 2 or 3. The Gaussian profile shown in Figure 3 is constrained to have the same center and 1240 km s^{-1} dispersion as the Si II 1260 Å feature. Visually, at least, the fit appears satisfactory.

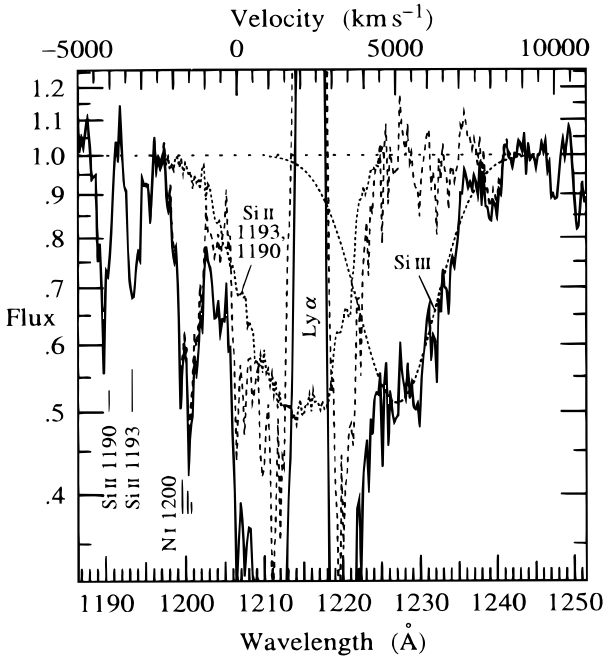

FIG. 2.—*HST* G130H spectrum (*solid line*) relative to the adopted stellar continuum around the redshifted Si III 1206.500 Å ($f = 1.669$) feature. Upper axis shows velocity in the rest frame of the Si III line. The position and width of the fitted Gaussian profile of Si III (*dotted line*) have been constrained to be the same as that of the Si II 1260 Å feature. Also shown is the residual (*dashed line*) after subtraction both of the Si III fitted Gaussian and of the contribution of redshifted Si II 1193, 1190 Å (*dotted line*) assumed to have the same profile as the Si II 1260 Å feature. The residual shows, besides Lyα emission and absorption, a weak indication of absorption by unshocked Si III at velocities 5500–7000 km s^{-1}. The adopted stellar continuum is the same as that for the Si II 1260 Å feature in Fig. 1.

TABLE 2

COLUMN DENSITIES OF SHOCKED AND UNSHOCKED Si III AND Si IV, RELATIVE TO BEST-FIT COLUMN DENSITIES OF Si II

Type	Si II	Si III	Si IV
Shocked.....	1 ± 0.03	0.43 ± 0.02	0.41 ± 0.02
Unshocked.....	1 ± 0.13	0.065 ± 0.035	0.02 ± 0.07

NOTES.—Absolute column densities of shocked and unshocked Si II are given in Table 1. Column densities of Si IV relative to Si II are for fits in which the dispersion of Si IV is constrained to be that of Si II 1260 Å, namely 1240 km s^{-1}. The column densities of Si IV become 0.46 ± 0.02 (shocked) and -0.06 ± 0.06 (unshocked) if instead the dispersion of the Si IV is taken to have the best-fit value 1700 ± 100 km s^{-1}.

2.7. *Total* Si *Mass*

In § 2.5, we showed that the observed column density of shocked Si II is close to the theoretical steady state value. Is the same also true for Si III and Si IV? The answer is no. In steady state, the predicted column densities of shocked ionic species are inversely proportional to their respective col-

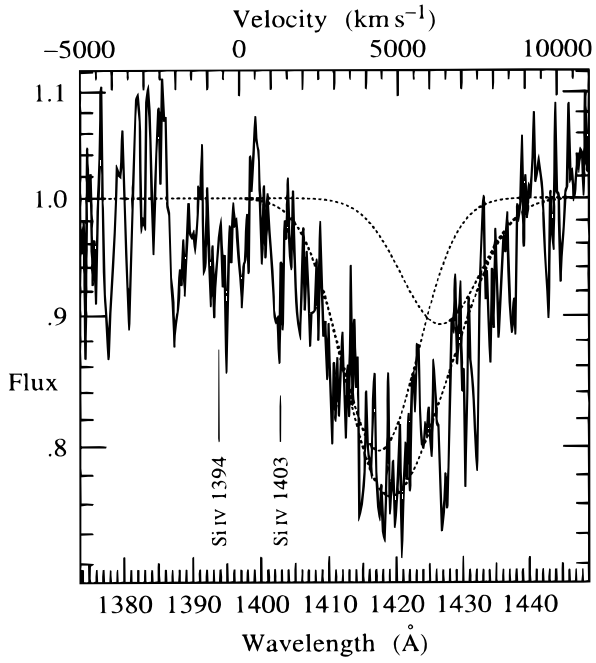

FIG. 3.—*HST* G130H spectrum relative to the adopted stellar continuum around the redshifted Si IV 1393.755, 1402.770 Å ($f = 0.5140, 0.2553$) feature. Upper axis shows velocity in the rest frame of the weighted mean wavelength of the feature. Dotted lines show the best fit to a Gaussian pair with line center and dispersion constrained to be that of Si II 1260 Å for each component of the doublet, and with optical depths fixed equal to the ratio of oscillator strengths times wavelengths of the doublet. The best-fit dispersion of the Si IV is 1700 ± 100 km s^{-1}, which is 4.5 σ larger than the 1240 km s^{-1} dispersion of the fit shown here. There is no evidence of unshocked Si IV. The adopted stellar continuum is $\log F = \log (2.9 \times 10^{-14}$ ergs s^{-1} cm^{-2} Å$^{-1}) - 1.4 \log (\lambda/1397$ Å).

lisional ionization rates $\langle \sigma v \rangle$, modified by an appropriate electron to ion ratio (see eq. [13]). Adopting rates 6.1×10^{-8} cm^3 s^{-1}, 2.2×10^{-8} cm^3 s^{-1}, and 1.1×10^{-8} cm^3 s^{-1} for Si II, Si III, and Si IV, respectively (Lennon et al. 1988) and assuming a nominal i electrons per ion for Si^{+i}, yields relative column densities in steady state

$$N_{\rm Si\,II}:N_{\rm Si\,III}:N_{\rm Si\,IV} = 1:1.4:1.8 \ . \qquad (15)$$

By comparison, the observed shocked column densities are $N_{\rm Si\,II}:N_{\rm Si\,III}:N_{\rm Si\,IV} = 1:0.43:0.41$, according to Table 2. Evidently, the observed abundances of shocked Si III and Si IV relative to Si II are several times less than predicted in steady state.

As discussed in § 2.5, there are several ways to reduce the column density below the steady state value, of which the most obvious is to truncate the column density, as is strongly suggested by the fact that the ionization timescales of Si III and Si IV are becoming long compared to the age of the remnant. In fact, these ionization timescales are in precisely the same ratio (see eq. [2]) as the steady state column densities (eq. [15])

$$t_{\rm Si\,II}:t_{\rm Si\,III}:t_{\rm Si\,IV} = 1:1.4:1.8 \ , \qquad (16)$$

and it has already been seen that the ionization timescale $t_{\rm Si\,II}$ of Si II is comparable to the age of the remnant, equation (3).

If it is true that it is the long ionization times that cause the column densities of Si III and Si IV to be lower than steady state, then this suggests that there may be little Si in higher ionization states in the shocked gas on the far side of SN 1006. Thus, it appears plausible that we are observing in UV absorption essentially all the Si there is on the far side of SN 1006 along the line of sight to the background SM star. To avoid confusion, it should be understood that this statement refers specifically to Si on the far side along this particular line of sight. Higher ionization states of Si are indicated by the observed Si X-ray line emission (Koyama et al. 1995), which could arise from denser shocked gas in other parts of the remnant.

The mass of Si can be inferred from the observed column densities of Si II, Si III, and Si IV if it is assumed that silicon was ejected spherically symmetrically by the supernova explosion. We will argue in § 2.8 that the absence of blueshifted absorbing Si is not inconsistent with spherical symmetry. Taking the shocked and unshocked masses of Si II from Table 1 and the ratios of Si II, Si III, and Si IV from Table 2 yields a total inferred Si mass of

$$M_{\rm Si} = 0.127(1 + 0.43 + 0.41)\ M_\odot + 0.017(1 + 0.065)\ M_\odot$$
$$= 0.25 \pm 0.01\ M_\odot \ . \qquad (17)$$

This is comparable to the 0.16 $M_\odot$ of Si in model W7 of Nomoto et al. (1984). It is also consistent with the 0.20 $M_\odot$ of Si inferred from the strength of the Si K line observed with *ASCA* (Koyama et al. 1995). Koyama et al. do not quote a mass, but they do state that the measured surface brightness of the Si K line is 5 times higher than that in the model[2] of Hamilton, Sarazin, & Szymkowiak (1986; see also Hamilton et al. 1985), which had 0.04 $M_\odot$ of Si.

2.8. *No Blueshifted* Si—*Evidence for an Inhomogeneous ISM?*

There is no evidence for blueshifted Si absorption in the UV spectrum. At best, there is a possible hint of a broad shallow depression around ~ -5000 km s^{-1}, from 1365 Å to 1390 Å, on the blue side of the Si IV 1394, 1403 Å line (see WCHFLS97, Fig. 1). The possibility that some high-velocity blueshifted Si II 1260 Å is hidden in the red wing of Si III 1206 Å is excluded by the absence of corresponding blueshifted Si II 1527 Å.

There are two possible reasons for the asymmetry in the observed Si absorption. One is that there was an intrinsic asymmetry in the supernova explosion. According to Garcia-Senz & Woosley (1995), the nuclear runaway that culminates in the explosion of a nearly Chandrasekhar mass white dwarf begins as stable convective carbon burning, and ignition is likely to occur off-center at one or more points over a volume of the order of a pressure scale height. The subsequent propagation of the convectively driven burning front is Rayleigh-Taylor unstable (Livne 1993; Khokhlov 1995; Niemeyer & Hillebrandt 1995), although Arnett & Livne (1994) find that in delayed detonation models the second, detonation, phase of the explosion tends to restore spherical symmetry.

[2] Hamilton et al. took the strength of the Si K line to be (the upper limit to) that measured from the *Einstein* Solid State Spectrometer (SSS) (Becker et al. 1980), so there is a discrepancy between the *ASCA* and SSS data. However, Hamilton et al. also noted in their Fig. 6 a marked discrepancy between the SSS and *HEAO-1* data of Galas, Venkatesan, & Garmire (1982), so it is reasonable to suspect an error in the normalization of the SSS data.

Thus, asymmetry in the explosion is possible, perhaps even likely, as an explanation of the asymmetry in the Si absorption, especially since the absorption samples only a narrow line of sight through SN 1006 to the background SM star. However, we do not pursue this possibility further, in part because in abandoning spherical symmetry we lose any predictive power, and in part because there is another explanation which is more attractive because it resolves some other observational problems.

The other possible cause of the asymmetry in the Si absorption is that the ISM around SN 1006 is inhomogeneous, with the ISM on the far side of SN 1006 having a significantly lower density than the near side. According to this hypothesis, the low density on the far side is such that the reverse shock on the far side has reached inward only to a free expansion radius of 7070 km s^{-1}, whereas the higher density on the near side is such that the reverse shock on the near side has passed entirely through the Si layer, and Si has been collisionally ionized to stages higher than Si IV, which makes it unobservable in UV absorption.

A serious objection to the reverse shock on the near side being farther in than the reverse shock on the far side is the observation by WCFHS93 of blueshifted Fe II absorption certainly to velocities -7000 km s^{-1}, perhaps to velocities -9000 km s^{-1}. We will review the observational evidence for such high velocity blueshifted Fe II in § 3 below, where we will argue that the evidence is not compelling.

An inhomogeneous ISM around SN 1006 is indicated by other observations. Wu et al. (1983) and subsequent authors have remarked on the difficulty of fitting the observed high-velocity (~ 7000 km s^{-1}) Si within the confines of the observed interstellar blast wave, if spherical symmetry is assumed. At a distance of 1.8 ± 0.3 kpc (Laming et al. 1996), the remnant's observed 15′ radius (Reynolds & Gilmore 1986, 1993; see also Willingale et al. 1996) at 980 yr old[3] corresponds to a free expansion radius of 7700 ± 1300 km s^{-1}. The difficulty is resolved if the remnant of SN 1006 bulges out on the far side, because of the lower density there.

A second piece of evidence that suggests inhomogeneity is the high 5050 km s^{-1} velocity of the shocked ejecta behind the reverse shock on the far side of SN 1006 inferred from the present observations, compared with the 1800–2400 km s^{-1} (the lower velocity corresponds to no collisionless electron heating, which is the preferred case) velocity of shocked gas behind the interstellar shock inferred from Hα and UV emission-line widths along the northwest sector of the remnant (Kirshner et al. 1987; Long et al. 1988; Smith et al. 1991; Raymond et al. 1995). These two velocities, 5050 km s^{-1} versus 1800–2400 km s^{-1}, appear incompatible, especially as the velocity of shocked gas is expected in realistic hydrodynamic models to increase outward from the reverse shock to the interstellar shock (see, for example, HF88, Fig. 2). The incompatibility is resolved if the ISM around SN 1006 is inhomogeneous, with the density on the far side of SN 1006 being substantially lower than the density at the northwest edge.

A final piece of evidence supporting inhomogeneity comes from the observation of Si K line emission in X-rays (Koyama et al. 1995). This emission is likely to be from ejecta, since the inferred abundance of Si is stated to be an order of magnitude higher than that of O, Ne, or Fe. To ionize Si to high ionization states in the age of SN 1006, and to produce Si K line emission at the observed luminosity, requires densities $n_{\rm Si} \gtrsim 10^{-2}$ cm^{-3} (i.e., $n_e \gtrsim 10^{-1}$ cm^{-3} since the Si is highly ionized), substantially higher than the postshock density of $n_{\rm Si\,II} = 2 \times 10^{-4}$ cm^{-3} deduced here from the redshifted Si II 1260 Å absorption profile. It is difficult to see how the required high Si density could be achieved if the reverse shock everywhere around the remnant is at a radius as high as 7070 km s^{-1}, whereas higher densities would occur naturally if the reverse shock around most of the remnant were farther in, since then ejecta would have been shocked at earlier times when its density ($\propto t^{-3}$ in free expansion) was higher.

All these arguments point to the notion that the ISM density on the far side of SN 1006 is anomalously low compared to the density around the rest of the remnant.

2.9. *Ionization of* Si *on the Near Side*

In § 3, we will argue that the Fe II absorption profiles suggest that the reverse shock on the near side of SN 1006 may be at a free expansion radius of 4200 km s^{-1} (as with the Hubble expansion of the universe, it is often convenient to think in a comoving frame expanding freely with the ejecta, so that a free expansion velocity $v = r/t$ can be thought of as a radius). Here we estimate whether Si could have ionized beyond Si IV, as required by the absence of observed blueshifted Si absorption, if the reverse shock on the near side is indeed at 4200 km s^{-1}.

In our first estimate, we find that blueshifted Si IV *should* be observable, with a column density $\sim 40\%$ that of the observed redshifted Si IV absorption. However, the column density is somewhat sensitive to the assumptions made, and it is not hard to bring the column density down below observable levels.

The line profile of any blueshifted absorbing Si would have a width comparable to that of the observed broad redshifted Si absorption, but the centroid would be shifted to lower velocities, to ~ -2000 km s^{-1}, if it assumed that the reverse shock velocity on the near side is comparable to that, $v_s = 2860$ km s^{-1}, observed on the far side. To avoid being observed at, say, 3 σ, the column density of blueshifted Si IV should be less than 0.6×10^{14} cm^{-2}.

To estimate the ionization of Si, it is necessary to adopt a hydrodynamic model. Now one interesting aspect of hydrodynamical models of deflagrated white dwarfs expanding into a uniform ambient medium is that the reverse shock velocity v_s remains almost constant in time (this conclusion is based on hydrodynamic simulations carried out by HF88). In model W7 of Nomoto et al. (1984), the reverse shock velocity varies (nonmonotonically) between 3300 km and 5200 km s^{-1} as it propagates inward from a free expansion radius of 13,000 to 700 km s^{-1}, after which the shock velocity accelerates. Similarly in model CDTG7 (S. E. Woosley 1987, private communication), which is similar to model CDTG5 of Woosley & Weaver (1987), the reverse shock velocity varies between 3200 and 4100 km s^{-1} as it propagates inward from a free expansion radius of 10,000 to 1500 km s^{-1}. These numbers do not depend on the density of the ambient medium, although they do depend on the ambient density being uniform. If the reverse shock velocity v_s remains constant in time, then the radius r of the reverse shock evolves with time t according to $dr/dt = r/t - v_s$,

[3] Note there is a 23 yr light-travel time across one radius of the remnant, so really we are seeing the far side at an age 23 yr younger, and the near side 23 yr older, than the mean age.

from which it follows that the free expansion radius r/t of the reverse shock varies with time as

$$\frac{r}{t} = v_s \ln\left(\frac{t_*}{t}\right), \tag{18}$$

where t_* is the age at which the reverse shock eventually hits the center of the remnant.

The assumption that the reverse shock v_s is constant in time may not be correct for SN 1006, but it provides a convenient simplification to estimate the ionization of Si on the near side. Let us first estimate the ionization state of Si that was originally at a free expansion radius of 7070 km s^{-1}, the current location of the reverse shock on the far side. If the reverse shock on the near side is currently at a free expansion radius of $r/t = 4200$ km s^{-1}, and if it has moved at a constant $v_s = 2860$ km s^{-1}, the measured value on the far side (recall that the reverse shock velocity is independent of the ambient density, for uniform ambient density), then it would have passed through a free expansion radius of 7070 km s^{-1} when the age t_s of SN 1006 was $t_s/t = \exp$ [(4200 km s^{-1} − 7070 km s^{-1})/2860 km s^{-1}] = 0.37 times its present age t, according to equation (18). The postshock density of Si ions at that time would have been $(t/t_s)^3 = 20$ times higher than the presently observed postshock density of $n_{\rm Si\ II} = 2.2 \times 10^{-4}$ cm^{-3}. The ion density in the parcel of gas shocked at that time has been decreasing because of adiabatic expansion. The rate of decrease of density by adiabatic expansion can be inferred from the observed global rate of expansion of the remnant (Moffet et al. 1993)

$$R \propto t^{\alpha},\ \alpha = 0.48 \pm 0.13\ , \tag{19}$$

which for an assumed uniform ambient density would imply that the pressure is decreasing as $P \propto (R/t)^2 \propto t^{2\alpha-2}$; hence, that the density in Lagrangian gas elements is varying as $n \propto P^{3/5} \propto t^{6(\alpha-1)/5}$. The current ionization time $\tau \equiv \int_{t_s}^{t} n dt$ of the parcel of gas originally at free expansion radius 7070 km s^{-1} that was shocked at an age $t_s/t = 0.37$ is then

$$\tau = \frac{n_{\rm Si\ II}\, t}{(6\alpha-1)/5}\left(\frac{t}{t_s}\right)^2\left[\left(\frac{t}{t_s}\right)^{(6\alpha-1)/5} - 1\right]$$
$$= 6.0 \times 10^7\ {\rm cm}^{-3}\ {\rm s}\ , \tag{20}$$

where $n_{\rm Si\ II}\, t = 6.6 \times 10^6$ cm^{-3} s is the present postshock density of Si II ions times age at the radius 7070 km s^{-1}. If the Si is assumed unmixed with other elements and initially singly ionized, then the ionization time (eq. [20]) yields ion fractions 5% Si III, 34% Si IV, and the remaining 61% in higher stages.

Since this ionization state is close to (just past) the peak in the Si IV fraction, it should be a good approximation to estimate the column density of Si IV by expanding locally about the conditions at 7070 km s^{-1}. The expected column density is the steady state column density, multiplied by a geometric factor, and further multiplied by a "density profile" factor $[1 + \gamma\tau/(n_s t_s)]^{-1}$, as shown in the Appendix, equation (A7). The steady column density is $N_{\rm Si\ IV}^{\rm steady} = n_{\rm Si\ IV} v_s/(4n_e\langle\sigma v\rangle_{\rm Si\ IV}) = 22 \times 10^{14}$ cm^{-2} assuming a nominal $n_e/n_{\rm Si\ IV} = 3$. The geometric factor is $(7070t_s/4200t)^2 = 0.38$, which is the squared ratio of the radius of the gas at the time t_s it was shocked to its radius at the present time t. For the density profile factor, equation (20) gives $\tau/(n_s t_s) = [(t/t_s)^{(6\alpha-1)/5} - 1]/[(6\alpha-1)/5] = 1.22$, while the logarithmic slope $\gamma = -\partial \ln n/\partial \ln t_s|_t$ of the shocked density profile, equation (A3), is $\gamma = 3 + v_s \partial \ln n^{\rm unsh}/\partial(r/t) + 6(\alpha-1)/5 = 3.7$, the 3 coming from free expansion, the $v_s \partial \ln n^{\rm unsh}/\partial(r/t) = 1.37$ from the observed unshocked Si II density profile (see eq. [27]) at 7070 km s^{-1} along with equation (18), and the $6(\alpha-1)/5 = -0.62$ from the reduction in density caused by adiabatic expansion. The resulting density profile factor is $[1 + \gamma\tau/(n_s t_s)]^{-1} = 0.18$. The expected column density of blueshifted Si IV is then $N_{\rm Si\ IV} = 1.5 \times 10^{14}$ cm^{-2}, which is 40% of the observed column density of redshifted Si IV, and 2.5 times the minimum (3 σ) observable column density of blueshifted Si IV.

Thus, under a reasonable set of simplifying assumptions, there should be an observable column density of blueshifted Si IV, contrary to observation. However, the expected column density is sensitive to the assumed parameters. For example, reducing the shock velocity on the near side by 20% to 2300 km s^{-1} reduces the column density by a factor 2.5 to the observable limit $N_{\rm Si\ IV} = 0.6 \times 10^{14}$ cm^{-2}. Whether the shock velocity on the near side is less or more than that on the far side depends on the unshocked density profile of ejecta (generally, a shorter exponential scale length of unshocked density with velocity yields lower shock velocities). The expected column density is also sensitive to the shocked density profile, as might be guessed from the fact that the density profile factor of 0.18 estimated above differs substantially from unity.

Alternatively, the column density of Si IV could be reduced below the observable limit by mixing the Si with a comparable mass of other elements, such as iron, since this would increase the number of electrons per silicon ion, causing more rapid ionization. The possibility that there is iron mixed with Si at velocities $\lesssim$7070 km s^{-1} gains some support from the observed density profile of Fe II, shown in Figure 6 below. Note that this does not conflict with the argument in § 2.5 that most of the shocked Si (which was originally at higher free expansion velocities) is probably fairly pure, with little admixture of other elements such as iron.

3. IRON

We have argued above that an attractive explanation for the presence of redshifted Si absorption and absence of blueshifted absorption is that the ISM on the near side of SN 1006 is much denser than that on the far side, so that a reverse shock has already passed all the way through the Si layer on the near side, ionizing it to high ionization stages, whereas the reverse shock is still moving through the Si layer on the far side. This picture appears to conflict with our previously reported result (WCFHS93), according to which blueshifted Fe II is present to velocities ~ -8000 km s^{-1}. In this section we reexamine the Fe II absorption lines to see how robust is this result.

In the average broad Fe II profile shown in Figure 3 of WCFHS93, redshifted Fe II seems to extend up to about 7000 km s^{-1}, but not much farther. This is consistent with the argument of the present paper, which is that the reverse shock on the far side of SN 1006 lies at 7070 km s^{-1}. The problem lies on the blueshifted side of the Fe II profile, which appears to extend clearly to -7000 km s^{-1}, possibly to -9000 km s^{-1}.

Figure 2 of WCFHS93 shows separately the two broad Fe II 2383, 2344, 2374 Å and Fe II 2600, 2587 Å features. The Fe II 2600, 2587 Å feature appears to have a fairly abrupt

blue edge, although there is perhaps a tail to higher velocities depending on where the continuum is placed. The blue edge is at a velocity of -4200 km s^{-1} with respect to the stronger 2600 Å component of the doublet, and the same edge appears at this velocity in the average Fe II profile shown in WCFHS93's Figure 3. We will argue that this edge plausibly represents the position of the reverse shock on the near side of SN 1006.

In contrast to Fe II 2600 Å, the deconvolved profile of the Fe II 2383 Å feature, plotted in the bottom curve of WCFHS93's Figure 2, shows blueshifted absorption clearly extending to $\lesssim 7000$ km s^{-1}. We note that the second strongest component of the triplet, 2344 Å, with one-third the oscillator strength of the principal 2383 Å component, lies at -4900 km s^{-1} blueward of the principal line, and uncertainty involved in removing the secondary component in the deconvolution procedure could tend to obscure any sharp blue edge at -4200 km s^{-1} on the principal component.

3.1. Fe II *Analysis*

In this subsection we present details of a reanalysis of the Fe II absorption lines in the *HST* G190H and G270H spectra originally analyzed by WCFHS93. The observations are described by WCFHS93, and here we describe the differences between the analysis here and that of WCFHS93. In carrying out the reanalysis, we paid particular attention to procedures that might affect the blue wing of the Fe II 2383 Å feature.

The G190H and G270H spectra overlap over the wavelength range 2222–2330 Å, and we merged the two spectra in this region using inverse variance weighting, whereas WCFHS93 chose to abut the spectra at 2277 Å. In merging the spectra, we interpolated the G270H data to the same bin size as the G190 spectrum, which has higher resolution (2 Å versus 2.8 Å), and higher signal-to-noise ratio than the G270H spectrum in the overlap region. According to the FOS handbook, there is contamination at the level of a few percent in the G190H spectrum above 2300 Å from second order, but, given the absence of strong features over 1150–1165 Å, we accept this contamination in the interests of obtaining higher signal-to-noise ratio. The merged spectrum is noticeably less choppy than the G270H spectrum alone in the overlap region.

The 2200 Å extinction bump is close to the blue wing of the Fe II 2383 Å feature, so we reexamined the reddening correction. In practice, the changes made here had little effect on the profile of the Fe II 2383 Å feature. We dereddened the G190H and G270H spectra using the extinction curve of Cardelli, Clayton, & Mathis (1989), adopting $E_{B-V} = 0.119$, which is the best-fitting value determined by Blair et al. (1996) from HUT data, and $R \equiv A_V/E_{B-V} = 3.0$. The value of E_{B-V} is slightly higher than the value $E_{B-V} = 0.1 \pm 0.02$ measured by WCFHS93 using the extinction curve of Savage & Mathis (1979). WCFHS93 comment that their dereddening leaves a bump from 1900 to 2100 Å and a shallow trough from 2100 to 2300 Å. We find the same difficulty here: the slightly higher value of E_{B-V} adopted here does slightly better at removing the 2200 Å depression but at the expense of producing a bigger bump at 2000 Å. The choice of R makes little difference, but lower values help to reduce the bump marginally. The value $R = 3.0$ adopted here is slightly below the "standard" value $R = 3.1$.

WCFHS93 fitted the continuum flux to a quadratic function of wavelength. The simple quadratic form does impressively well in fitting the dereddened spectrum over the full range 1600–3300 Å (see Fig. 4 and WCFHS93, Fig. 2). However, the quadratic form does not fit perfectly, and there remains a residual discrepancy that is not well fitted by a low-order polynomial and that may possibly result from imperfect modeling of the extinction, especially around the 2200 Å bump. The imperfection mainly affects the Fe II 2383 Å feature: the quadratic continuum appears too steep compared to the "true" continuum around this feature. Here we resolve the difficulty by the expedient of fitting the dereddened continua around each of the two broad Fe II features separately to two different linear functions in log F– log λ. The adopted continua are shown in Figure 4.

An important difference between the present analysis and that of WCFHS93 is in the treatment of narrow lines. WCFHS93's procedure was to identify all lines with an equivalent width, defined relative to a local continuum, greater than 3 times the expected error. WCFHS93 then subtracted the best-fitting Gaussian for each such line, treating the position, width, and strength of each line as free parameters. Here we adopt a different policy, requiring that the positions, widths, and strengths of narrow lines conform to prior expectation. That is, for each identified narrow line, we subtract a Gaussian profile in which the wavelength is set equal to the expected wavelength (modulo an overall $+36$ km s^{-1} shift for all lines), the width is set equal to the instrumental resolution (2.8 Å FWHM for G270H), and the strengths are required to be mutually consistent with other narrow lines of the same ion.

The relevant narrow lines are those in and near the broad Fe II features. In the Fe II 2383, 2344, 2374 Å feature, besides the narrow (presumed interstellar) components of the Fe II lines themselves, we identify the narrow line at 2298 Å as stellar C III 2297.578 Å (Bruhweiler, Kondo, & McCluskey 1981). WCFHS93 subtracted an unidentified narrow line at 2316 Å, but the G190H spectrum does not confirm the reality of this line in the G270H spectrum, and here we leave it unsubtracted. In the Fe II 2600, 2587 Å feature, besides the narrow Fe II lines themselves, we identify narrow lines of Mn II 2577, 2594, 2606 Å, as did WCFHS93.

The mean velocity shift of the three most prominent narrow Fe II lines, those at 2383, 2600, and 2587 Å, is $+36 \pm 24$ km s^{-1}, and we adopt this velocity shift for all the narrow Fe II and Mn II lines. We allow the stellar C III 2298 Å line its own best-fit velocity shift of $+19$ km s^{-1}, since there is no reason to assume that the stellar and interstellar velocities coincide exactly.

The observed equivalent widths of the Mn II lines are approximately proportional to their oscillator strengths times wavelengths, which suggests the lines are unsaturated, so we fix the ratios of the fitted Mn II lines at their unsaturated values.

Of the five narrow Fe II lines, the two principal lines Fe II 2383 Å and Fe II 2600 Å, and also the line with the fourth largest oscillator strength, Fe II 2587 Å, have approximately equal observed equivalent widths (in velocity units) relative to a local continuum, W_{2383}, W_{2600}, $W_{2587} = 85 \pm 6$ km s^{-1}, 64 ± 6 km s^{-1}, 62 ± 6 km s^{-1}, respectively (at fixed centroid and dispersion), which suggests the lines are saturated. The fifth and weakest line, Fe II 2374 Å, has an observed equivalent width about half that of the strong

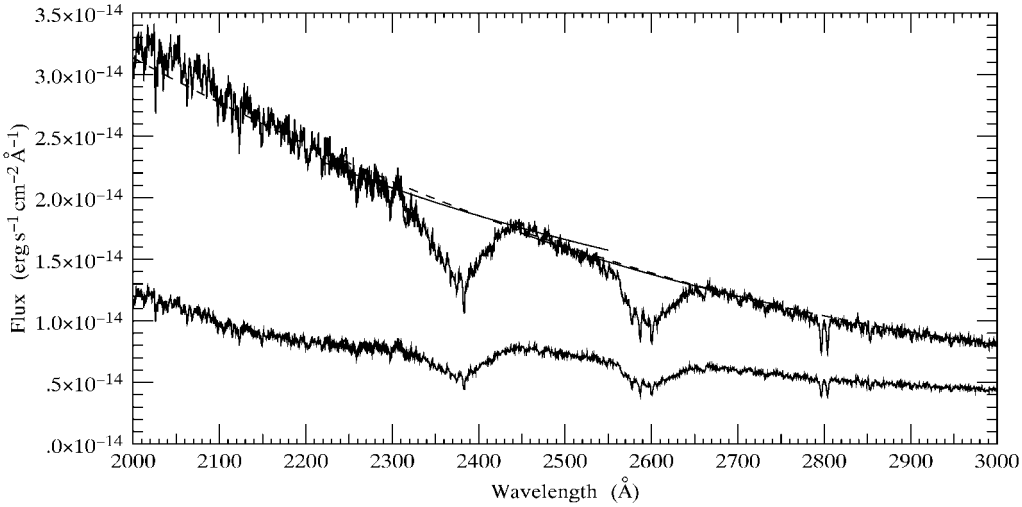

FIG. 4.—G190H and G270H spectra, with the calibrated spectra at bottom and the dereddened spectra at top. Also shown are the continua linear in log F– log λ (*solid lines*) adopted in the present paper for each of the Fe II 2600 Å and Fe II 2383 Å features, and a continuum quadratic in F-λ (*dashed line*) similar (but not identical, because of the slightly different reddening) to that adopted by WCFHS93. The linear continua are log F = log (1.89×10^{-14} ergs s^{-1} cm^{-2} Å^{-1}) − 2.7 log (λ/2383 Å) for the Fe II 2383 Å feature, and log F = log (1.38×10^{-14} ergs s^{-1} cm^{-2} Å^{-1}) − 3.65 log (λ/2600 Å) for the Fe II 2600 Å feature.

lines, which is consistent with the weak line being marginally optically thin and the strong lines again being saturated. For these four lines, we allow the strength of the fitted line to take its best-fit value, since they are mutually consistent within the uncertainties.

The line with the third largest oscillator strength, Fe II 2344 Å, appears anomalous, since the observed line has an equivalent width less than one-fourth that of the strong lines, or one-half that of the intrinsically weaker Fe II 2374 Å line. In the fit, we force the equivalent width of the anomalous Fe II 2344 Å narrow line to be the saturated value measured from the Fe II 2600 Å and Fe II 2587 Å lines, multiplied by 0.8 to allow for a 2 σ uncertainty in this value. The fit gives the impression that the anomalous Fe II 2344 Å line is oversubtracted, but the effect is to bring the profile of the deconvolved broad Fe II 2383 Å line into closer agreement with that of Fe II 2600 Å.

We deconvolved the broad Fe II 2383, 2344, 2374 Å and Fe II 2600, 2587 Å features by subtracting the contributions from the weaker components, using the following analytic procedure. In a two-component line, the observed optical depth $\tau(v)$ at velocity v with respect to the principal component is a sum of the line profile $\phi(v)$ of the principal component and the line profile $\epsilon\phi(v + \Delta v)$ of the secondary component, where Δv is the velocity shift of the secondary relative to the principal component, and $\epsilon = f_2\lambda_2/(f_1\lambda_1) < 1$ is the ratio of oscillator strengths times wavelengths:

$$\tau(v) = \phi(v) + \epsilon\phi(v + \Delta v) \, . \tag{21}$$

Equation (21) inverts to

$$\phi(v) = \tau(v) - \epsilon\tau(v + \Delta v) + \epsilon^2\tau(v + 2\Delta v) + \ldots \, , \tag{22}$$

which can conveniently be solved iteratively by

$$\begin{aligned} \phi_1(v) &= \tau(v) - \epsilon\tau(v + \Delta v) \, , \\ \phi_{n+1}(v) &= \phi_n(v) + \epsilon^{2^n}\phi_n(v + 2^n\Delta v) \, . \end{aligned} \tag{23}$$

The iterative procedure converges rapidly to the solution, $\phi_n \to \phi$, as n increases; we stop at ϕ_3. To avoid irrelevant parts of the spectrum outside the line profile from propagating through the solution, we set the optical depth to zero, $\tau(v) = 0$ in equation (23), at velocities $v > 10,000$ km s^{-1}. The above procedure works for a two-component line such as Fe II 2600, 2587 Å, and a slightly more complicated generalization works for a three-component line such as Fe II 2383, 2344, 2374 Å.

3.2. Fe II *Line Profiles*

Figure 5 shows the results of our reanalysis. Table 3 summarizes some of the measured parameters. The upper curves in the figure show the deconvolved Fe II 2383 Å and Fe II 2600 Å line profiles, and these deconvolved profiles agree well with each other. The deconvolved Fe II 2600 Å profile here also agrees well with that of WCFHS93. However, the revised Fe II 2383 Å profile no longer shows compelling evidence for high-velocity blueshifted absorption beyond −4500 km s^{-1}, although the presence of some absorption is not excluded.

What causes the difference between the Fe II 2383 Å line profile shown in Figure 5 versus that of WCFHS93? One factor is that we adopt different continua, as illustrated in Figure 4. WCFHS93's single quadratic fit to the continuum over the entire spectrum is certainly more elegant than the two separate linear fits to each of the two broad Fe II features that we adopt here. The advantage of the fit here is that it removes the apparent tilt in the Fe II 2383 Å line profile left by the quadratic fit, evident in Figures 2 and 3 of WCFHS93.

However, the major difference between the two analyses

TABLE 3

PARAMETERS MEASURED FROM Fe II PROFILE

Parameter	Value
Position of reverse shock on near side...	-4200 ± 100 km s^{-1}
Column density of Fe II	$10.8 \pm 0.9 \times 10^{14}$ cm^{-2}
Mass of Fe II up to 7070 km s^{-1}.....	0.029 ± 0.004 $M_\odot$

NOTE.—Fe II mass is from red side of profile and assumes spherical symmetry.

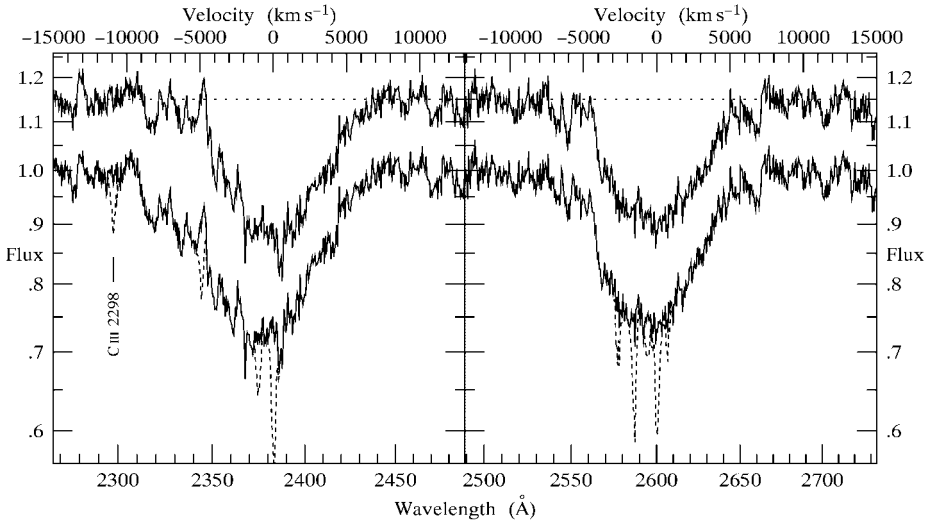

FIG. 5.—Fe II 2382.765, 2344.214, 2374.4612 Å ($f = 0.3006$, 0.1097, 0.02818; we ignore an unobserved fourth component Fe II 2367.5905 Å with $f = 1.6 \times 10^{-4}$) feature, and at right the Fe II 2600.1729, 2586.6500 Å ($f = 0.2239$, 0.06457) feature (Morton 1991). Below 2330 Å, the spectrum is an inverse-variance–weighted merger of G190H and G270H spectra. The lower curve shows the dereddened spectrum, scaled to a continuum, with narrow interstellar Fe II, stellar C III 2297.578 Å, and interstellar Mn II 2576.877, 2594.499, 2606.462 Å ($f = 0.3508$, 0.2710, 0.1927) lines subtracted as indicated by dashed lines. The upper curve (offset by log 1.15) shows the deconvolved spectra, after removal of the weaker components of the broad Fe II lines. The velocity scales shown on the upper axis are with respect to the rest frames of the principal component of each of the features, the Fe II 2383 Å line on the left, and the Fe II 2600 Å line on the right. The adopted continua are as shown in Fig. 4.

is the subtraction here of the narrow Fe II 2344 Å interstellar line with a strength 0.8 times the saturated line strength observed in the Fe II 2600 Å and 2587 Å narrow lines. By comparison, WCFHS93 subtracted the narrow Fe II 2344 Å line using the observed strength of the line, which is anomalously weak compared to the other four narrow Fe II lines.

Figure 6 shows the Fe II density inferred from the mean of the two deconvolved Fe II features. The Fe II column density inferred from the mean profile, integrated from -4500 km s^{-1} to $+7100$ km s^{-1}, is

$$N_{\rm Fe\,II} = 10.8 \pm 0.9 \times 10^{14}\ {\rm cm}^{-2}\ . \qquad (24)$$

Most of the uncertainty, based here on the scatter between the two deconvolved profiles, comes from the blue side of the profile: the column density on the blue side from -4500 to 0 km s^{-1} is $N_{\rm Fe\,II} = 5.2 \pm 0.8 \times 10^{14}$ cm^{-2}, while the column density on the red side from 0 to $+7100$ km s^{-1} is $N_{\rm Fe\,II} = 5.6 \pm 0.2 \times 10^{14}$ cm^{-2}.

In estimating the mass of Fe II from the density profile in Figure 6, we take into account the small correction that results from the fact that the SM star is offset by 2.″45 ± 0.″25 southward from the projected center of the 15′ radius remnant (Schweizer & Middleditch 1980). The offset corresponds to a free expansion velocity of $v_\perp = 1300 \pm 250$ km s^{-1} at the 1.8 ± 0.3 kpc distance of the remnant. If spherical symmetry is assumed, then the mass is an integral over the density $\rho(v)$ at line-of-sight velocity v:

$$M = M(<v_\perp) + t^3 \int_0^{v_{\rm max}} \rho(v)(v^2 + v_\perp^2)^{1/2} v\, dv\ , \qquad (25)$$

where $M(<v_\perp)$ is the mass inside the free-expansion velocity $v_\perp$. At a constant central density of $\rho_{\rm Fe\,II} = 0.005 \times 10^{-24}$ g cm^{-3}, the mass inside $v_\perp = 1300$ km s^{-1} would be $M_{\rm Fe\,II}(<v_\perp) = 0.0007\ M_\odot$, and the actual Fe II mass is probably slightly higher, given that the density is increasing mildly inward. The masses given below, equation (26), include a fixed $M_{\rm Fe\,II}(<v_\perp) = 0.001\ M_\odot$. The factor $(v^2 + v_\perp^2)^{1/2}$ rather than v in equation (25) increases the Fe II masses by a further $0.002\ M_\odot$, so the masses quoted in equation (26) are altogether $0.003\ M_\odot$ larger than they would be if no adjustment for the offset of the SM star were applied.

The total mass of Fe II inferred from the cleaner, red side

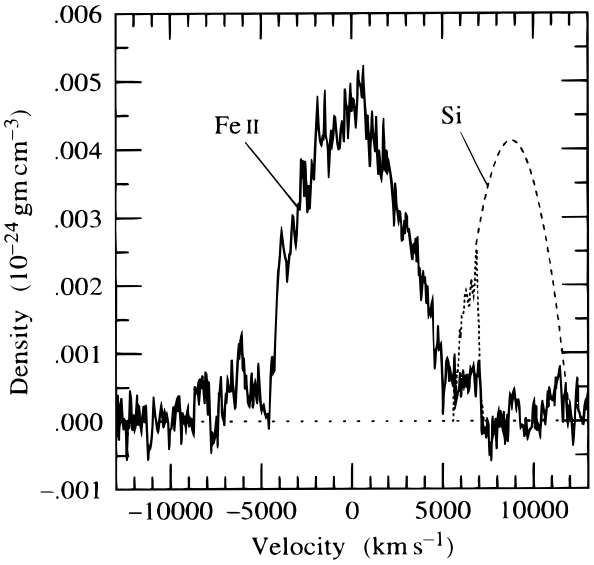

FIG. 6.—Inferred density profile of ejecta in SN 1006. The Fe II profile is from the mean of the two deconvolved broad Fe II absorption features shown in Fig. 5. The dotted line at $+5600$–7070 km s^{-1} is the profile of unshocked Si II from the redshifted Si II 1260 Å absorption feature in Fig. 1. The dashed line above 7070 km s^{-1} is a plausible extrapolation of the total Si density before it was shocked: it is a quadratic function of velocity, eq. (27), which approximately reproduces the observed profile of unshocked Si II, and which contains the observed total Si mass of $0.25\ M_\odot$ (assuming spherical symmetry), eq. (17).

of the profile, assuming spherical symmetry, is then

$$M_{\rm Fe\ II} = \begin{cases} 0.0156 \pm 0.0009\ M_\odot & (v \le 4200\ {\rm km\ s^{-1}}) \\ 0.0195 \pm 0.0013\ M_\odot & (v \le 5000\ {\rm km\ s^{-1}}) \\ 0.029 \pm 0.004\ M_\odot & (v \le 7070\ {\rm km\ s^{-1}}) \, . \end{cases} \quad (26)$$

Note that these are total Fe II masses, even though only the red side of the profile is used to estimate them. The uncertainties here are based on the scatter between the two deconvolved Fe II profiles and do not include systematic uncertainties arising from placement of the continuum, which mostly affects the outer, high-velocity parts of the profile. WCFHS93 obtained a total $M_{\rm Fe\ II} = 0.014\ M_\odot$ from the red side of the mean Fe II profile, which is lower than the $M_{\rm Fe\ II} = 0.029\ M_\odot$ obtained here mainly because of the different placement of the continuum, especially on the red side of the Fe II 2383 Å feature (see Fig. 4, and compare Fig. 5 to WCFHS93, Fig. 3), and to a small degree because of the adjustment applied here for the offset of the SM star.

Figure 6 also shows for comparison the density of unshocked Si. Below 7070 km s^{-1}, the Si density profile is just the unshocked profile inferred from the Si II 1260 Å absorption, Figure 1. Above 7070 km s^{-1}, the Si density is a plausible extrapolation that is consistent with observational constraints: it is a quadratic function of the free expansion velocity v

$$n_{\rm Si} = 0.00413 \times 10^{-24}\ {\rm g\ cm^{-3}} \times \frac{(v - 5600\ {\rm km\ s^{-1}})(12{,}000\ {\rm km\ s^{-1}} - v)}{(3200\ {\rm km\ s^{-1}})^2} \, , \quad (27)$$

which approximately reproduces the observed profile of unshocked Si II and which contains, on the assumption of spherical symmetry, a total Si mass of 0.25 $M_\odot$, in accordance with equation (17).

3.3. *Reverse Shock on the Near Side*

If the reanalysis of the Fe II lines here is accepted, then it is natural to interpret the sharp blue edge on the broad Fe II lines at -4200 km s^{-1} as representing the free expansion radius of the reverse shock on the near side of SN 1006. This identification is not as convincing as the identification of the sharp red edge on the Si II 1260 Å feature as representing the radius of the reverse shock on the far side at 7070 km s^{-1}.

Figure 7 illustrates schematically the inferred structure of the remnant of SN 1006. The picture is intended to be approximately to scale, and in it the diameter of SN 1006 along the line of sight is roughly 20% larger than the diameter transverse to the line of sight. By comparison, the diameter of the observed radio and X-ray remnant varies by 10%, from a minimum of 30′ to a maximum of 33′ (Reynolds & Gilmore 1986, 1993) or 34′ (Willingale et al. 1996).

As already discussed in §§ 2.8 and 2.9, if the position of the reverse shock on the near side at 4200 km s^{-1} is typical of the rest of the remnant, while the 7070 km s^{-1} position of the reverse shock on the far side is anomalously high because the interstellar density on the far side is low, then it would resolve several observational puzzles. In summary, these observational puzzles are (1) how to fit gas expanding at $\sim$7000 km s^{-1} within the confines of the interstellar shock (answer: the remnant bulges out on the far side because of the low density); (2) how the 5050 km s^{-1} velocity of shocked Si on the far side could be so much higher than the 1800 km s^{-1} velocity (assuming no collisionless electron heating) of gas behind the interstellar shock along the northwest filament (answer: velocities on the far side are anomalously high because the interstellar density there is anomalously low); (3) how to achieve Si densities $n_{\rm Si} \gtrsim 10^{-2}$ cm^{-2} necessary to produce the observed Si X-ray emission, compared to the postshock Si density of 2.2×10^{-4} cm^{-2} measured from the Si II absorption on the far side (answer: gas shocked at earlier times is denser because density decreases as $\rho \propto t^{-3}$ in free expansion); and (4) why there is strong redshifted Si absorption but no blueshifted absorption (answer: Si on the near side has been shocked and collisionally ionized above Si IV). As regards the second of these problems, if the reverse shock on the near side is indeed at 4200 km s^{-1}, then the velocity of reverse-shocked gas on the near side would be of order 2000 km s^{-1}, much more in keeping with the 1800 km s^{-1} velocity of shocked gas in the northwest filament.

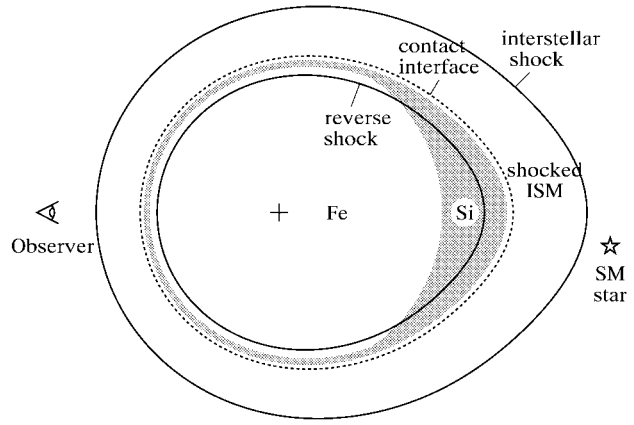

FIG. 7.—Schematic diagram, approximately to scale, of the structure of the remnant of SN 1006 inferred in this paper. The remnant on the far side bulges out because of the low interstellar density there. Shaded regions represent silicon ejecta, both shocked and unshocked. Iron, both shocked and unshocked, lies inside the silicon. The background SM star is offset slightly from the projected center of the remnant.

3.4. *Contribution of Shocked Fe to Absorption*

In §§ 2.1 and 2.6, we concluded that most of the observed absorption by Si ions is from shocked Si. Does shocked Fe also contribute to the observed broad Fe II absorption profiles? The answer, on both observational and theoretical grounds, is probably not much.

On the red side of the Fe II profile, shocked Fe II would have a Gaussian line profile centered at 5050 km s^{-1}, the same as observed for shocked Si. No absorption with this profile is observed; see Figures 5 or 6. Since the collisional ionization rates of Fe II and Si II are similar (Lennon et al. 1988), the absence of such Fe II absorption implies that there cannot be much iron mixed in with the shocked Si. This is consistent with the argument in § 2.5, that the bulk of the shocked Si II must be fairly pure, unmixed with other elements.

On the other hand, the observed Fe II profile, Figure 6, does suggest the presence of some Fe II mixed with unshocked Si, at velocities $\lesssim$7070 km s^{-1}. The picture then is that there is Fe mixed with Si at lower velocities but not

at higher velocities. This is consistent with SN Ia models, such as W7 of Nomoto et al. (1984), in which the transition from the inner Fe-rich layer to the Si-rich layer is gradual, rather than abrupt.

On the blue side of the Fe II profile, if the reverse shock is at -4200 km s^{-1}, then shocked Fe II should have a Gaussian profile centered at ~ -2000 km s^{-1}, with a width comparable to that of the broad redshifted Si features. While some such absorption may be present, the similarity between the blueshifted and redshifted sides of the Fe II absorption suggests that the contribution to the blue side from shocked Fe II is not large. This is consistent with expectation from the density profile of unshocked Fe II on the red side. The mass of Fe II at velocities 4200–7070 km s^{-1} inferred from the red side of the profile on the assumption of spherical symmetry is $0.013\ M_\odot$. If this mass of Fe II is supposed shocked on the blue side and placed at the reverse shock radius of -4200 km s^{-1}, the resulting Fe column density is 1.3×10^{14} cm^{-2}, which translates into a peak Fe density of 0.0013×10^{-24} g cm^{-3} at velocity -2200 km s^{-1}, for an assumed dispersion of 1240 km s^{-1} like that of the redshifted Si features. This density of shocked Fe is low enough that it makes only a minor contribution to the Fe II profile in Figure 6.

In practice, collisional ionization of shocked Fe II reduces its contribution further. For pure iron with an initial ionization state of, say, 50% Fe II, 50% Fe III (see § 3.5), we find that the column density of shocked Fe II is reduced by a factor 0.6 to 0.8×10^{14} cm^{-2}, which translates into a peak Fe II density of 0.0008×10^{-24} g cm^{-3} at velocity -2200 km s^{-1}. The shocked column density would be even lower if the initial ionization state is higher, or if there are other elements mixed in with the Fe, since a higher electron–to–Fe II ratio would make collisional ionization faster. If the initial ionization state of the iron is as high as proposed by HF88, then the shocked Fe II column density of Fe could be as low as 0.1×10^{14} cm^{-2}, for a peak density of 0.0001×10^{-24} g cm^{-3} at velocity -2200 km s^{-1} in Figure 6.

3.5. *Photoionization*

The mass of Fe II inferred here from the Fe II profile is, according to equation (26), $0.0195 \pm 0.0013\ M_\odot$ up to 5000 km s^{-1}, and $0.029 \pm 0.004\ M_\odot$ up to 7070 km s^{-1}.

Historical and circumstantial evidence suggests that SN 1006 was a Type Ia supernova (Minkowski 1966; Schaefer 1996). Exploded white dwarf models of Type Ia supernovae predict that several tenths of a solar mass of iron ejecta should be present, as required to explain Type Ia supernova light curves (Höflich & Khokhlov 1996). Thus, as emphasized by Fesen et al. (1988) and by HF88, the observed mass of Fe II in SN 1006 is only a fraction ($\lesssim 1/10$) of the expected total Fe mass.

Hamilton & Sarazin (1984) pointed out that unshocked SN ejecta will be subject to photoionization by UV starlight and by UV and X-ray emission from the reverse shock. Recombination is negligible at the low densities here. HF88 presented detailed calculations of the time-dependent photoionization of unshocked ejecta in SN 1006, using deflagrated white dwarf models W7 of Nomoto et al. (1984) and CDTG7 of S. E. Woosley (1987, private communication), evolved by hydrodynamic simulation into a uniform interstellar medium. HF88 found that in these models most of the unshocked Fe was photoionized to Fe III, Fe IV, and Fe V. While model W7 produced considerably more Fe II than observed in SN 1006, model CDTG7, which is less centrally concentrated than W7, produced an Fe II profile in excellent agreement with the *IUE* Fe II 2600 Å feature. HF88 concluded that several tenths of a solar mass of unshocked Fe could be present at velocities $\lesssim 5000$ km s^{-1} in SN 1006, as predicted by Type Ia supernova models.

However, the low ionization state of unshocked Si inferred from the present *HST* observations does not support the high ionization state of Fe advocated by HF88. According to the ion fractions given in Table 2, unshocked Si is $92\% \pm 7\%$ Si II. By comparison, HF88 argued that unshocked Fe is only $\sim 10\%$ Fe II. We now show that these ionization states of Si II and Fe II are not mutually consistent.

The ionizations of unshocked Si II and Fe II are related according to their relative photoionization cross sections and by the energy distribution of the photoionizing radiation. Neutral Si and Fe can be neglected here, since they have ionization potentials below the Lyman limit and are quickly ionized by UV starlight (Si I in ~ 20 yr, Fe I in ~ 100 yr if the starlight is comparable to that in the solar neighborhood), once the ejecta start to become optically thin to photoionizing radiation, at ~ 100–200 yr.

Photoionization cross sections of Si II and Fe II, taken from Reilman & Manson (1979) and adapted to include autoionizing photoionization as described by HF88, are shown in Figure 8. The Figure shows that the photoionization cross section of Fe II is about an order of magnitude larger than that of Si II from the ionization potential up to the L-shell (autoionizing) photoionization threshold of Si II at 100 eV, above which the photoionization cross sections are about equal, until the L-shell threshold of Fe II at 700 eV. According to HF88 (Table 6, together with Table 2 of Hamilton & Sarazin 1984), much of the photoionizing emission from the reverse shock is in the UV below 100 eV. However, there is also some soft X-ray emission above 100 eV, which is important for Si II because its L-shell photoionization cross section is larger than that of the valence shell. Averaging over the photoionizing photons tabulated by HF88, we find that the effective photoionization cross section of Fe II is about 5 times that of Si II, which is true whether the source of the emission in the reverse shock is oxygen, silicon, or iron.

If the effective photoionization cross section of Fe II is 5 times that of Si II, then an unshocked Si II fraction of 0.92 ± 0.07 would predict an unshocked Fe II fraction of $(0.92 \pm 0.07)^5 = 0.66^{+0.29}_{-0.22}$, considerably larger than the desired unshocked Fe II fraction of 0.1. The 3 σ lower limit on the Si II fraction is 0.71, which would predict an unshocked Fe II fraction of $(0.71)^5 = 0.18$, closer to but still higher than desired.

A higher ionization state of Fe compared to Si might be achieved if the photoionizing emission could be concentrated entirely in the UV below 100 eV, since then the effective photoionization cross section of Fe II would be about 10 times that of Si II, as illustrated in Figure 8. This could occur if the photoionizing emission were mainly from He. In this case, the predicted unshocked Fe II fraction would be $(0.92 \pm 0.07)^{10} = 0.43^{+0.47}_{-0.27}$, with a 3 σ lower limit of $(0.71)^{10} = 0.03$, which is satisfactory. To achieve this relatively high level of Fe ionization requires that there be little soft X-ray emission from heavy elements. It is not clear

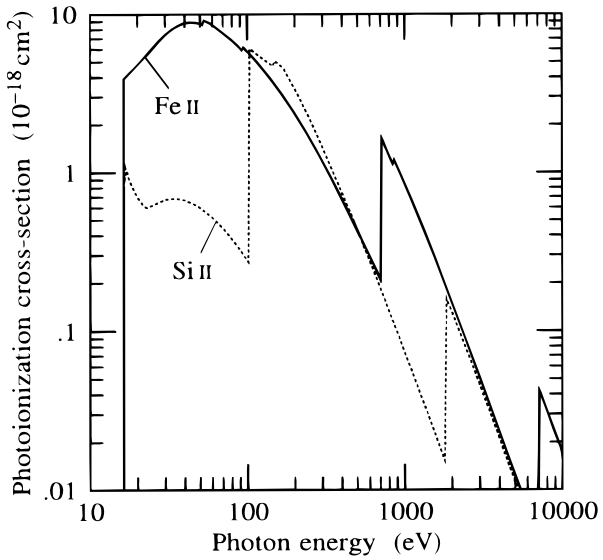

FIG. 8.—Photoionization cross sections of Si II and Fe II (Reilman & Manson 1979, adapted to include autoionizing photoionization as described by HF88). The ionization state of unshocked ejecta depends on photoionization, and the plotted photoionization cross sections are important in relating the ionization state of unshocked iron, characterized by the ratio Fe II/Fe, to the ionization state of unshocked silicon, characterized by the ratio Si II/Si.

whether this is possible, given the observed X-ray emission from oxygen and silicon (Koyama et al. 1995).

Thus the low ionization state of unshocked Si inferred in this paper is difficult to reconcile with the expected presence of several tenths of a solar mass of Fe at velocities $\lesssim 5000$ km s^{-1}. Is it possible that the unshocked Si is substantially more ionized than we have inferred? From Tables 1 and 2, the total column densities of Si ions, shocked and unshocked, are in the ratio

$$N_{\rm Si\,II}:N_{\rm Si\,III}:N_{\rm Si\,IV} = 1:0.39:0.36\ . \qquad (28)$$

If the ionization state of the unshocked Si were this high, then a high ionization state of Fe would be allowed, and the problem would be resolved. In fact, in photoionization trials similar to those described by HF88, we find that the unshocked Si fractions predicted by the CDTG7 model are close to the ratio (eq. [28]).

However, in § 2.6, we argued both theoretically and from the observed line profiles that most of the observed Si III and Si IV absorption is from shocked Si. Might this be wrong, and could in fact much or most of the absorption be from unshocked Si? And is then our interpretation of the Si II 1260 Å profile as arising mostly from shocked Si II also faulty? If so, then much of the tapestry of reasoning in this paper begins to unravel. For example, we must regard as merely coincidental the agreement, found in § 2.2, of the measured parameters of the Si II 1260 Å profile with the energy shock jump condition, equations (4)–(6). We must also conclude that the observed asymmetry between the red and blueshifted Si absorption arises from asymmetry in the initial explosion, not (or not all) from asymmetry in the ambient ISM. For if the blue edge of the redshifted Si II and Si IV features (the blue edge of redshifted Si III is obscured by Lyα) arises from unshocked Si extending down to velocities $+2500$ km s^{-1} (see Figs. 1 and 3), then there should be, on the assumption of spherical symmetry, corresponding blueshifted Si absorption outward of -2500 km s^{-1}, which is not seen.

3.6. *Where Is the Iron?*

Höflich & Khokhlov's (1996) Table 1 presents a survey of 37 Type Ia supernova models, encompassing all currently discussed explosion scenarios. In their models, the ejected mass of ^{56}Ni, which decays radioactively to iron, ranges from 0.10 to 1.07 $M_\odot$. Models yielding "acceptable" fits to the sample of 26 Type Ia supernovae considered by Höflich & Khokhlov have ejected ^{56}Ni masses of 0.49–0.83 $M_\odot$ for normal Type Ia supernovae and 0.10–0.18 $M_\odot$ for subluminous Type Ia superovae. In the subluminous models, a comparable amount of Fe is ejected along with the ^{56}Ni (Höflich, Khokhlov, & Wheeler 1995), so the total iron ejected in these cases is ≈ 0.2–$0.3\ M_\odot$.

In the previous subsection, we argued that the low ionization state of unshocked Si inferred from the present observations suggests that the ionization state of unshocked Fe is also likely to be low. Specifically, if the unshocked Si II fraction is Si II/Si $= 0.92 \pm 0.07$, from Table 1, then the predicted unshocked Fe II fraction is Fe II/Fe $= 0.66^{+0.29}_{-0.22}$. Correcting the Fe II mass of $M_{\rm Fe\,II} = 0.029 \pm 0.004\ M_\odot$ up to 7070 km s^{-1}, equation (26), for the ionization state of the Fe yields a total inferred Fe mass of $M_{\rm Fe} = 0.044^{+0.022}_{-0.013}\ M_\odot$ up to 7070 km s^{-1}, with a 3 σ upper limit of $M_{\rm Fe} < 0.16\ M_\odot$. These Fe masses are lower than predicted by either normal or subluminous models of Type Ia supernovae.

A low ionization state of Fe is supported by the HUT observations of Blair et al. (1996), who looked for Fe III 1123 Å absorption in the background SM star. If there is a large mass of Fe in SN 1006, significantly larger than the observed Fe II mass, then certainly Fe III should be more abundant than Fe II, and from detailed models, HF88 predicted Fe III/Fe II $= 2.6$. Blair et al.'s best fit is Fe III/Fe II $= 1.1 \pm 0.9$, and their 3 σ upper limit is Fe III/Fe II < 3.8. This result does not support, though it does not yet definitely exclude, HF88's prediction.

Neither of the above two observational evidences favoring a low ionization state of Fe, hence a low mass of Fe in SN 1006, is yet definitive. To settle the issue will require reobservation of the Fe III 1123 Å line at a higher signal-to-noise ratio. The *FUSE* should accomplish this.

4. WORRIES

In this paper we have attempted to present a consistent theoretical interpretation of the broad Si and Fe absorption features in SN 1006. While the overall picture appears to fit together nicely, the pieces of the jigsaw do not fit perfectly everywhere. In this section we highlight the ill fits.

What causes the discrepancy between the profiles of the redshifted Si II 1260 Å and Si II 1527 Å features? This discrepancy was originally pointed out and discussed for the *IUE* data by Fesen et al. (1988), and the discrepancy remains in the *HST* data (WCHFLS97). The discrepancy is especially worrying for the present paper because the excess in the Si II 1260 Å profile compared to Si II 1527 Å (see WCHFLS97, Fig. 2) looks a lot like what we have interpreted here as the unshocked component of the Si II 1260 Å absorption (Fig. 1).

We have argued that the redshifted Si II, Si III, and Si IV absorption is caused mostly by shocked Si, yet it is not clear that the observed relative column densities are naturally reproduced in collisionally ionized gas. Specifically, one

might expect relatively more Si III, or relatively less Si II or Si IV, in the shocked Si. On the other hand, the observed relative column densities of Si are naturally reproduced in unshocked, photoionized gas. Is our interpretation at fault?

The best-fit dispersion of the redshifted Si IV feature, Figure 3, is 1700 ± 100 km s^{-1}, which is 4.5 σ larger than that of the Si II 1260 Å feature, 1240 ± 40 km s^{-1}. What causes this discrepancy?

Does the density of shocked Si vary a little or a lot? In § 2.1, we argued that the Gaussian profile of the shocked Si suggests little temperature variation, hence little density variation. On the other hand, the unshocked Si density profile below 7070 km s^{-1} (Fig. 1) suggests a density profile increasing steeply outward, and there are other clues hinting at the same thing: the large column density of shocked Si II, § 2.5, and the need for a high density to ionize Si on the near side above Si IV, § 2.9. Is there an inconsistency here?

In § 2.5, we argued that the high observed column density of shocked Si II indicates a low mean electron–to–Si II ratio, $n_e/n_{\rm Si\ II} \lesssim 1.3$; equation (14). Higher ratios would cause more rapid collisional ionization of Si II, which would reduce the column density below what is observed. This limit on the electron–to–Si II ratio is satisfactory as it stands (the limit is somewhat soft, and at least it is not less than 1), but it is uncomfortably low, which makes it difficult to admit even modest quantities of other elements, such as sulfur, which might be expected to be mixed with the silicon. Is there a problem here, and if so have we perhaps overestimated the contribution of shocked compared to unshocked Si in the Si II absorption?

In § 2.9, we estimated that if the reverse shock on the near side of SN 1006 is at -4200 km s^{-1}, then under a "simplest" set of assumptions, there should be an observable column density of blueshifted Si IV, contrary to observation. However, we also showed that the predicted column density is sensitive to the assumptions and that it is not difficult to bring the column density of Si IV below observable levels. Is this explanation adequate, or does the absence of blueshifted Si absorption hint at asymmetry in the supernova explosion?

Is the sharp blue edge on the Fe II features at -4200 km s^{-1} real? Further observations of the Fe II features at higher resolution would be helpful in deciding this issue.

Notwithstanding our reanalysis of the Fe II features, there remains some suggestion of high-velocity blueshifted absorption outside -4200 km s^{-1}, perhaps to -7000 km s^{-1} or even farther, Figures 5 and 6. Is this absorption real? If so, then the arguments of § 2.8 fail, and the absence of blueshifted Si absorption must be attributed to intrinsic asymmetry in the initial supernova explosion.

Finally, there is the problem discussed in § 3.6: where is the iron?

5. SUMMARY

We have presented a consistent interpretation of the broad Si and Fe absorption features observed in SN 1006 against the background SM star (Schweizer & Middleditch 1980).

We have argued that the strong redshifted Si II 1260 Å absorption feature arises from both unshocked and shocked Si, with the sharp red edge of the feature at 7070 km s^{-1} representing the free expansion radius of the reverse shock on the far side of SN 1006, and the Gaussian blue edge signifying shocked Si (Fig. 1). Fitting to the Si II 1260 Å line profile yields three velocities, the position of the reverse shock, and the velocity and dispersion of the shocked gas, which permits a test of the energy jump condition for a strong shock. The measured velocities satisfy the condition remarkably well, equations (4)–(6). The Si II 1260 Å line thus provides direct evidence for the existence of a strong shock under highly collisionless conditions.

The energy jump condition is satisfied provided that virtually all the shock energy goes into ions. This evidence suggests little or no collisionless heating of electrons in the shock, in agreement with recent evidence from UV line widths and strengths (Raymond et al. 1995; Laming et al. 1996).

The observed column density of shocked Si II is close to the column density expected for steady state collisional ionization behind a shock, provided that the electron–to–Si II ion ratio is low. From the low electron–to–Si II ratio, we have argued that the shocked Si is probably of a fairly high degree of purity, with little admixture of other elements. More directly, the absence of Fe II absorption with the same line profile as the shocked Si indicates that there is little Fe mixed with the shocked Si. On the other hand, there is some indication of absorption by Fe II at the velocity 5600–7070 km s^{-1} of the unshocked Si II, which suggests that some Fe is mixed with Si in the lower velocity region of the Si layer.

We have proposed that the ambient interstellar density on the far side of SN 1006 is anomalously low compared to the density around the rest of the remnant, so that the remnant bulges out on the far side (Fig. 7). This would explain several observational puzzles. First, it would explain the absence of blueshifted Si absorption matching the observed redshifted Si absorption. If the interstellar density on the near side is substantially larger than on the far side, then the reverse shock on the near side would be farther in, so that all the Si on the near side could have been shocked and collisionally ionized above Si IV, making it unobservable in absorption. Second, if the velocity on the far side is anomalously high because of the low interstellar density there, it would resolve the problem noted by Wu et al. (1983) and subsequent authors of how to fit gas expanding at $\sim$7000 km s^{-1} within the confines of the interstellar shock. Third, a low density on the far side would explain how the 5050 km s^{-1} velocity of shocked Si there could be so much higher than the 1800 km s^{-1} velocity (assuming no collisionless electron heating) of gas behind the interstellar shock along the northwest filament (Smith et al. 1991; Raymond et al. 1995). Finally, the density of Si on the far side inferred from the Si absorption profiles is 1 or 2 orders of magnitude too low to yield Si X-ray emission at the observed level (Koyama et al. 1995). Again, an anomalously low density on the far side is indicated.

The notion that the reverse shock on the near side has moved inward much farther, to lower velocities, than on the far side conflicts with our earlier conclusion (WCFHS93) that there is blueshifted Fe II absorption to velocities ~ -8000 km s^{-1}. Reanalyzing the Fe II data, we find that the evidence for such high-velocity blueshifted Fe II absorption is not compelling. In the WCFHS93 analysis, the main evidence for high-velocity blueshifted Fe II comes from the Fe II 2383, 2344, 2374 Å feature. However, the 2344 Å component, which lies at -4900 km s^{-1} relative to the principal 2383 Å component, confuses interpretation of the blue wing of the feature. The Fe II 2600, 2587 Å feature is cleaner, and

it shows a sharp blue edge at -4200 km s^{-1}, which we interpret as representing the free expansion radius of the reverse shock on the near side of SN 1006. In our reanalysis of the Fe II features, we adopt a rigorous approach to the subtraction of narrow interstellar and stellar lines, requiring that lines subtracted have the correct positions and dispersions and have mutually consistent strengths. In particular, we subtract the narrow Fe II 2344 Å line with a strength consistent with the other narrow Fe II lines, which strength is substantially greater than the apparent strength. Subtraction of this line introduces a sharp blue edge on the deconvolved Fe II 2383, 2344, 2374 Å feature at the same place, ≈ -4200 km s^{-1}, as the Fe II 2600, 2587 Å feature. The resulting deconvolved Fe II profiles (Fig. 5) are in good agreement with each other.

The mass and velocity distribution of Si and Fe inferred in this paper provides useful information for modeling the remnant of SN 1006 (see Fig. 6). Freely expanding unshocked Si on the far side extends from a low velocity of 5600 ± 100 km s^{-1} up to the position of the reverse shock at 7070 km s^{-1}. Above this velocity, the Si is shocked, and information about its detailed velocity distribution before being shocked is lost. The total mass of Si, both unshocked and shocked, inferred from the Si II, Si III, and Si IV lines is $M_{\rm Si} = 0.25 \pm 0.01\ M_\odot$, on the assumption of spherical symmetry.

We have argued that the observed broad Fe II absorption arises almost entirely from unshocked freely expanding Fe. The mass of Fe II inferred from the cleaner, red side of the mean Fe II profile is $M_{\rm Fe\ II} = 0.0195 \pm 0.0013\ M_\odot$ up to 5000 km s^{-1} and $M_{\rm Fe\ II} = 0.029 \pm 0.004\ M_\odot$ up to 7070 km s^{-1}, again on the assumption of spherical symmetry. These masses include a small positive adjustment ($0.003\ M_\odot$) resulting from the offset of the SM star from the projected center of the remnant.

Our analysis of the Si lines indicates a low ionization state for the unshocked silicon, with Si II/Si $= 0.92 \pm 0.07$. Such a low state would imply a correspondingly low ionization state of unshocked iron, with Fe II/Fe $= 0.66^{+0.29}_{-0.22}$. If this is correct, then the total mass of Fe up to 7070 km s^{-1} is $M_{\rm Fe} = 0.044^{+0.022}_{-0.013}\ M_\odot$ with a 3 σ upper limit of $M_{\rm Fe} < 0.16\ M_\odot$. The absence of Fe II absorption with a profile like that of the shocked Si II suggests that there is not much more Fe at higher velocities. Such a low mass of Fe conflicts with the expectation that there should be several tenths of a solar mass of Fe in this suspected Type Ia supernova remnant. A low ionization state of Fe and a correspondingly low Fe mass is consistent with the low Fe III/Fe II $= 1.1 \pm 0.9$ ratio measured by Blair et al. (1996) from HUT observations of the Fe III 1123 Å line in the spectrum of the SM star. However, neither the present observations nor the HUT data are yet conclusive.

Reobservation of the Fe III 1123 Å line at higher signal-to-noise ratio with *FUSE* will be important in determining the ionization state of unshocked Fe in SN 1006, and in resolving the question, Where is the iron?

We would like to thank Bill Blair for helpful correspondence on the HUT data, and Graham Harper and Mike Shull for advice on respectively stellar and interstellar lines. Support for this work was provided by NASA through grant GO-3621 from the Space Telescope Science Institute, which is operated by AURA, Inc., under NASA contract NAS 5-26555.

APPENDIX A

IONIZATION TIMES IN NON–STEADY STATE

This Appendix demonstrates the assertion made in § 2.5, that the column density per interval of ionization time is reduced compared to the steady state value if the density of shocked gas increases downstream, and vice versa. The main result is equation (A7).

Define a collisional ionization time τ (not to be confused with optical depth) by the integral over time of the number density n in a Lagrangian gas element, from the time t_s when the gas element was first shocked, to the present time t:

$$\tau \equiv \int_{t_s}^{t} n dt\ . \tag{A1}$$

The density n in the definition (eq. [A1]) of the ionization time is the ion density. One might think to use the electron density n_e rather than the ion density, since the collisional ionization is by electron impact, but in fact the electron-to-ion ratio is itself determined by the ionization time, for any given initial ionization state, so there is no loss of generality in the definition (eq. [A1]).

It is useful to regard the shock age t_s as a Lagrangian coordinate labeling different gas elements. Then the ionization time τ of different gas elements at fixed time t varies according to

$$\left.\frac{\partial \tau}{\partial t_s}\right|_t = -n_s + \int_{t_s}^{t} \left.\frac{\partial n}{\partial t_s}\right|_t dt\ , \tag{A2}$$

where n_s is the postshock density at the time the gas was shocked. The minus sign in front of n_s reflects the fact that gas elements farther downstream were shocked at earlier times. If the pressure is spatially constant, which should be a good approximation, and if the gas density varies adiabatically as the pressure changes in time, then the densities n in different elements vary with time in proportion to each other. It follows that the logarithmic derivative of density n with respect to the Lagrangian coordinate t_s is independent of time. It is convenient to denote this dimensionless logarithmic derivative by γ:

$$\gamma(t_s) \equiv -\left.\frac{\partial \ln n}{\partial \ln t_s}\right|_t\ , \tag{A3}$$

which is positive if the density at fixed time t increases downstream. Then equation (A2) becomes

$$\left.\frac{\partial\tau}{\partial \ln t_s}\right|_t = -n_s t_s - \gamma\tau \ . \tag{A4}$$

Now consider the column density N contributed by gas elements shocked at different times t_s. The rate at which mass M of ions mass m enters the shock at time t_s, when the shock radius is r_s, is

$$\dot{M} = -\frac{dM}{dt_s} = 4\pi m r_s^2 n_s^{\rm presh} v_s = \pi m r_s^2 n_s v_s \ , \tag{A5}$$

the postshock density being 4 times the preshock density for a strong shock, $n_s = 4n_s^{\rm presh}$. The minus sign $-dM/dt_s$ here arises because we choose to label the interior mass $M(t_s)$ so that it increases downstream of the shock, in the direction of decreasing t_s. Mass is conserved in Lagrangian elements, and the column density N at time t when the shock radius is r varies with t_s as

$$\left.\frac{\partial N}{\partial \ln t_s}\right|_t = \frac{1}{4\pi m r^2}\frac{dM}{d\ln t_s} = -\frac{r_s^2}{r^2}\frac{n_s v_s t_s}{4} \ , \tag{A6}$$

which is diluted by the geometric factor r_s^2/r^2 compared to the column density at the time t_s when the gas was shocked.

Comparing the column density (A6) to the ionization time (A4) shows that the column density per interval of ionization time observed at a time t is

$$\left.\frac{\partial N}{\partial\tau}\right|_t = \frac{r_s^2 v_s}{4r^2}\frac{1}{[1+\gamma\tau/(n_s t_s)]} \ , \tag{A7}$$

which is the principal result of this Appendix. In steady state, equation (A7) reduces to $\partial N/\partial\tau|_t = v_s/4$. Compared to steady state, the non–steady state column density per unit ionization time (A7) thus contains two factors discussed in § 2.5, the geometric dilution factor r_s^2/r^2, and the density profile factor $[1+\gamma\tau/(n_s t_s)]^{-1}$. Since τ and $n_s t_s$ are always positive, this latter factor is less than or greater than 1 depending on whether γ, equation (A3), is greater than or less than zero. In other words, if the density n increases downstream, $\gamma > 0$, then the column density is reduced compared to steady state, and vice versa, as was to be proved.

REFERENCES

Arnett, D., & Livne, E. 1994, ApJ, 427, 330
Becker, R. H., Szymkowiak, A. E., Boldt, E. A., Holt, S. S., & Serlemitsos, P. J. 1980, ApJ, 240, L33
Blair, W. P., Long, K. S., & Raymond, J. C. 1996, ApJ, 468, 871
Bruhweiler, F. C., Kondo, Y., & McCluskey, G. E. 1981, ApJS, 46, 255
Cardelli, J. A., Clayton, G. C., & Mathis, J. S. 1989, ApJ, 345, 245
Chevalier, R. A., Blondin, J. M., & Emmering, R. T. 1992, ApJ, 392, 118
Fesen, R. A., & Hamilton, A. J. S. 1988, in A Decade of UV Astronomy with *IUE* (ESA SP-281) (Noordwijk: ESA), Vol. 1, p. 121
Fesen, R. A., Wu, C.-C., Leventhal, M., & Hamilton, A. J. S. 1988, ApJ 327, 164
Galas, C. M. F., Venkatesan, D., & Garmire, G. 1982, ApJ, 22, 103
Garcia-Senz, D., & Woosley, S. E. 1995, ApJ, 454, 895
Hamilton, A. J. S., & Fesen, R. A. 1988, ApJ, 327, 178 (HF88)
Hamilton, A. J. S., & Sarazin, C. L. 1984, ApJ, 287, 282
Hamilton, A. J. S., Sarazin, C. L., & Szymkowiak, A. E. 1986, ApJ, 300, 698
Hamilton, A. J. S., Sarazin, C. L., Szymkowiak, A. E., & Vartanian, M. H. 1985, ApJ, 297, L5
Höflich, P., & Khokhlov, A. 1996, ApJ, 457, 500
Höflich, P., Khokhlov, A. M., & Wheeler, J. C. 1995, 444, 831
Khokhlov, A. 1995, ApJ, 449, 695
Kirshner, R. P., Winkler, P. F., & Chevalier, R. A. 1987, ApJ, 315, L135
Koyama, K., Petre, R., Gotthelf, E. V., Hwang, U., Matsuura, M., Ozaki, M., & Holt, S. S. 1995, Nature, 378, 255
Laming, J. M., Raymond, J. C., McLaughlin, B. M., & Blair, W. P. 1996, ApJ, 472, 267
Lennon, M. A., Bell, K. L., Gilbody, H. B., Hughes, J. G., Kingston, A. E., Murray, M. J., & Smith, F. J. 1988, J. Phys. Chem. Ref. Data, 17, 1285
Livne, E. 1993, ApJ, 406, L17
Long, K. S., Blair, W. P., & van den Bergh, S. 1988, ApJ, 333, 749
Minkowski, R. 1966, AJ, 71, 371
Moffet, D. A., Goss, W. M., & Reynolds, S. P. 1993, AJ, 106, 1566
Morton, D. C. 1991, ApJS, 77, 119
Niemeyer, J. C., & Hillebrandt, W. 1995, ApJ, 452, 769
Nomoto, K., Thielemann, F.-K., & Yokoi, K. 1984, ApJ, 286, 644
Raymond, J. C., Blair, W. P., & Long, K. S. 1995, ApJ, 454, L31
Reilman, R. F., & Manson, S. T. 1979, ApJS, 40, 815
Reynolds, S. P. 1996, ApJ, 459, L13
Reynolds, S. P., & Gilmore, D. M. 1986, AJ, 92, 1138
———. 1993, AJ, 106, 272
Savage, B. D., & Mathis, J. S. 1979, ARA&A, 17, 73
Schaefer, B. E. 1996, ApJ, 459, 438
Schweizer, F., & Middleditch, J. 1980, ApJ, 241, 1039
Smith, R. C., Kirshner, R. P., Blair, W. P., & Winkler, P. F. 1991, ApJ, 375, 652
Willingale, R., West, R. G., Pye, J. P., & Stewart, G. C. 1996, MNRAS, 278, 749
Woosley, S. E., & Weaver, T. A. 1987, in IAU Colloq. 89, Radiation Hydrodynamics in Stars and Compact Objects, ed. D. Mihalas & K.-H. A. Winkler (Berlin: Springer), 91
Wu, C.-C., Crenshaw, D. M., Fesen, R. A., Hamilton, A. J. S., & Sarazin, C. L. 1993, ApJ, 416, 247 (WCFHS93)
Wu, C.-C., Crenshaw, D. M., Hamilton, A. J. S., Fesen, R. A., Leventhal, M., & Sarazin, C. L. 1997, ApJ, 447, L53 (WCHFLS97)
Wu, C.-C., Leventhal, M., Sarazin, C. L., & Gull, T. R. 1983, ApJ, 269, L5